

# Combining frequency-difference and ultrasound modulated electrical impedance tomography<sup>†</sup>

Bastian Harrach<sup>1</sup>, Eunjung Lee<sup>2</sup>, Marcel Ullrich<sup>1</sup>

<sup>1</sup> Department of Mathematics, University of Stuttgart, Germany

<sup>2</sup> Department of Computational Science and Engineering, Yonsei University, Seoul, Korea

E-mail: [harrach@math.uni-stuttgart.de](mailto:harrach@math.uni-stuttgart.de), [eunjunglee@yonsei.ac.kr](mailto:eunjunglee@yonsei.ac.kr), [marcel.ullrich@mathematik.uni-stuttgart.de](mailto:marcel.ullrich@mathematik.uni-stuttgart.de)

**Abstract.** Electrical impedance tomography (EIT) is highly affected by modeling errors regarding electrode positions and the shape of the imaging domain. In this work, we propose a new inclusion detection technique that is completely independent of such errors. Our new approach is based on a combination of frequency-difference and ultrasound modulated EIT measurements.

AMS classification scheme numbers: 35R30, 35J25

## 1. Introduction

The goal of electrical impedance tomography (EIT) is to image the conductivity inside a subject. To that end, electrodes are attached to the subject's boundary, and one measures the voltages that are required to drive a specified static or time-harmonic current through different combinations of the attached electrodes. The potential advantages of EIT compared to other imaging techniques are that conductivity values are typically of a high specificity, and that EIT devices are comparatively cheap and easily portable.

The inverse problem of reconstructing the conductivity from boundary voltage and current measurements is known to be highly non-linear and ill-posed. The measurements are very insensitive to changes in the conductivity values away from the electrodes. They do, however, strongly depend on the measurement geometry, i.e., the electrode position and the shape of the imaging domain. In most applications, it is not feasible to precisely measure the geometry, and electrodes are frequently placed by hand. Hence, such modeling or geometry errors present a major challenge for practical EIT applications.

---

<sup>†</sup> This is an author-created, un-copyedited version of an article published in *Inverse Problems* **31**(9), 095003, 2015. IOP Publishing Ltd is not responsible for any errors or omissions in this version of the manuscript or any version derived from it. The Version of Record is available online at <http://dx.doi.org/10.1088/0266-5611/31/9/095003>.

The main focus of EIT is often on the detection and localization of conductivity inclusions or anomalies (e.g., material faults or pathological regions) inside an otherwise more or less homogeneous medium.

In this work, we propose a new measurement setup for anomaly detection and describe a reconstruction method that is completely unaffected by geometrical modelling errors, as it does not require knowledge of the electrode position or the shape of the imaging domain.

The main idea of our new technique is to combine ultrasound-modulated EIT measurements with frequency-difference EIT measurements. We focus an ultrasound wave on a small region inside the imaging domain to alter the conductivity in the focusing region. The resulting effect on the EIT measurements is then compared to the effect of a change in the electric current frequency. This comparison shows whether the focusing region lies inside a conductivity anomaly or not.

To decide whether the focusing region lies inside an anomaly, our method utilizes only the two sets of EIT measurements (with ultrasound-modulation and after the frequency change) and the ratio of the background conductivity before and after the frequency change. The latter can be estimated from comparing EIT measurements before and after the frequency change, as it is done in weighted frequency-difference EIT (see the references below). The method can be implemented using simple monotonicity tests, i.e., the taken voltage measurements are arranged in the form of a matrix and then compared in the sense of matrix definiteness (resp., in the idealized case of continuous boundary measurements, the measurements are interpreted as Neumann-to-Dirichlet operators and compared in the sense of definiteness of self-adjoint compact operators).

Our new method does not use any forward simulations, or explicitly known special solutions, that would depend on the geometry of the setup. It does not require any knowledge of the electrode position or the shape of the imaging domain, and is hence completely unaffected by modeling errors.

We give a complete proof for our method for the case of continuous boundary data, when the measurements are given by the Neumann-to-Dirichlet-operator. For the case of measurements on a finite number of electrodes, we prove that the method correctly identifies the case where the focusing region lies inside the anomaly. We also give a physical justification (in the spirit of [36]), that regions outside the anomaly will correctly be identified if enough electrodes are used for the measurements, cf. remark 3.3.

Let us now comment on related works and the origins of our approach. For a broad overview on electrical impedance tomography see [39, 6, 13, 61, 16, 10, 11, 12, 60, 40, 40, 8, 1, 75, 64]. For the task of anomaly detection in EIT, let us refer to Friedmann and Isakov [20, 21] for early works, Potthast [65] for an overview on non-iterative methods, and [35] for the recent result that shape information is invariant under linearization. Iterative anomaly detection methods are commonly based on level-set approaches, cf., e.g. [52, 72, 18, 19, 77, 66]. Prominent non-iterative anomaly detection methods are the Factorization Method (see [54, 28, 22, 31, 43, 59, 63, 24, 27, 34, 67, 36, 68, 26, 15, 17, 7]

and the recent overviews [55, 30, 33]), the enclosure method (see [47, 14, 48, 50, 49, 51, 45, 76, 44]), and the recently emerging monotonicity method (see the references below).

Our new method is based on a monotonicity-based comparison of weighted frequency-difference EIT (fdEIT) and ultrasound-modulated EIT (UMEIT) measurements. Monotonicity-based comparisons were first considered as heuristic inclusion-detection methods and numerically tested by Tamburrino and Rubinacci [74, 73]. Recently, the monotonicity method was rigorously justified [38] using the concept of localized potentials [23]. Weighted fdEIT has been introduced in order to improve the reconstruction stability with respect to modeling errors in settings where no reference (anomaly-free) data is available, see [69, 34, 36]. The hybrid tomography technique UMEIT was introduced in [79, 2], cf. also [58, 3, 56, 57, 78, 4, 62, 5, 9] for more works on this subject. When the measurement geometry is known, UMEIT allows to measure the interior electrical energy of the subject by altering the conductivity with a focused ultrasound waves (cf. the related idea of Impedance-Acoustic Tomography [25], where interior energy data is obtained from measuring expansion effects caused by electrical heating). Knowledge of this additional interior energy information eliminates the major cause of ill-posedness in the reconstruction process, which could greatly increase image resolution. Moreover, let us mention that combinations of EIT and ultrasound have been studied that rely on data-fusion rather than on coupled physics, e.g., by using ultrasound images as prior information for EIT reconstructions, cf., e.g., [70, 71].

At this point, it has to be noted, that (up to the knowledge of the authors) the idea of using focused waves in ultrasound-modulated EIT (UMEIT) yet has to be experimentally validated. The results in this work are derived under the idealistic assumption of a perfectly focused ultrasound waves that changes the conductivity in a well-defined circular region. Of course, in reality, such a perfect focus cannot be realized, and the ultrasound wave will also affect the conductivity outside the focusing region. Moreover, the location of the focusing region will not be known exactly but depend on the measurement geometry. It is, however, widely accepted that in typical EIT applications, conductivity contrast is much higher than ultrasound contrast, while ultrasound resolution is much higher than EIT resolution. Therefore we believe that techniques relying on UMEIT are worth investigating despite the current lack of practical validation.

The paper is organized as follows. In section 2, we start with describing the general setting of complex conductivity EIT and ultrasound modulated EIT for continuous boundary data. Then we derive a monotonicity relation for complex conductivity EIT, and use this relation to develop an anomaly detection algorithm that is based on comparing EIT measurements at a non-zero frequency with ultrasound-modulated DC measurements. Section 3 contains the corresponding results for a setting with finitely many electrodes using the shunt electrode model. In section 4, we illustrate our new method with two- and three-dimensional numerical results. Section 5 concludes the paper with a discussion of our results.

## 2. Continuous boundary data

### 2.1. The setting

We start by describing the general setting of complex conductivity EIT and ultrasound modulated EIT with continuous boundary data. We consider a bounded imaging domain  $\Omega \subset \mathbb{R}^n$ ,  $n \geq 2$  with piecewise smooth boundary. For  $x \in \Omega$ , let

$$\gamma_\omega(x) = \sigma_\omega(x) + i\omega\epsilon_\omega(x)$$

denote the body's complex admittance at frequency  $\omega \geq 0$ . We assume that

$$\Re(\gamma_\omega) = \sigma_\omega \in L_+^\infty(\Omega; \mathbb{R}), \quad \text{and} \quad \Im(\gamma_\omega) = \omega\epsilon_\omega \in L^\infty(\Omega; \mathbb{R}),$$

where  $\Re(\cdot)$  and  $\Im(\cdot)$  denote the real and imaginary part, the subscript “+” indicates functions with positive (essential) infima, and throughout this work all function spaces consist of complex valued functions if not stated otherwise.

Complex EIT measurements consist of applying time-harmonic currents to the surface of the imaging domain and measuring the resulting electric surface potential. In the so-called continuum model (see, e.g., [16]), these measurements are described by the Neumann-to-Dirichlet-Operator

$$\Lambda(\gamma_\omega) : L_\diamond^2(\partial\Omega) \rightarrow L_\diamond^2(\partial\Omega), \quad g \mapsto u_{\gamma_\omega}^{(g)}|_{\partial\Omega},$$

where  $u_{\gamma_\omega}^{(g)} \in H_\diamond^1(\Omega)$  solves

$$\nabla \cdot (\gamma_\omega \nabla u_{\gamma_\omega}^{(g)}) = 0 \text{ in } \Omega \quad \text{and} \quad \gamma_\omega \partial_\nu u_{\gamma_\omega}^{(g)}|_{\partial\Omega} = g. \quad (1)$$

Here, the subspace of  $L^2(\partial\Omega)$  and  $H^1(\Omega)$ -functions with vanishing integral mean on  $\partial\Omega$  is denoted by  $L_\diamond^2(\partial\Omega)$  and  $H_\diamond^1(\Omega)$ , respectively.  $\nu$  is the outer normal on  $\partial\Omega$ . It is well known that  $\Lambda(\gamma_\omega)$  is a well-defined, linear and compact operator.

The idea of ultrasound-modulated EIT is to focus an ultrasound wave on a small part  $B \subseteq \Omega$  in order to change the density of the material and thus its conductivity in  $B$ , cf. [2]. A simple, very idealistic model is that the focused ultrasound wave changes the conductivity from  $\gamma_\omega$  to  $\gamma_\omega(1 + \beta\chi_B)$ , where  $\beta > 0$  depends on the strength of the ultrasound wave and  $\chi_B$  is the characteristic function of  $B$ . Hence, ultrasound-modulated EIT measurements can be modeled as

$$\Lambda(\gamma_\omega(1 + \beta\chi_B)).$$

In this work, we will compare measurements at a non-zero frequency  $\Lambda(\gamma_\omega)$ ,  $\omega > 0$ , with ultrasound-modulated DC measurements  $\Lambda(\gamma_0(1 + \beta\chi_B))$  in order to detect whether the ultrasound modulated part  $B$  lies inside a conductivity anomaly or not.

### 2.2. Monotonicity results for the continuous case

We will compare measurements in the sense of operator definiteness. Given a bounded linear operator  $A : L_\diamond^2(\partial\Omega) \rightarrow L_\diamond^2(\partial\Omega)$ , we define its self-adjoint part by setting

$$\Re(A) := \frac{1}{2}(A + A^*)$$

where  $A^* : L_\diamond^2(\partial\Omega) \rightarrow L_\diamond^2(\partial\Omega)$  is the adjoint of  $A$  with respect to the inner product of  $L_\diamond^2(\partial\Omega)$ , i.e.,

$$\int_{\partial\Omega} \bar{g}(Ah) \, ds = \int_{\partial\Omega} (\overline{A^*g})h \, ds \quad \text{for all } g, h \in L_\diamond^2(\partial\Omega).$$

Obviously,  $\Re(A)$  is a self-adjoint bounded linear operator.

For two self-adjoint bounded linear operators  $A, B : L_\diamond^2(\partial\Omega) \rightarrow L_\diamond^2(\partial\Omega)$ , we write  $A \leq B$  if  $B - A$  is positive semidefinite, i.e.

$$\int_{\partial\Omega} \bar{g}Ag \, ds \leq \int_{\partial\Omega} \bar{g}Bg \, ds \quad \forall g \in L_\diamond^2(\partial\Omega).$$

For compact operators, this is equivalent to the fact that all eigenvalues of  $B - A$  are non-negative.

Note that, for all  $g, h \in L_\diamond^2(\partial\Omega)$ , the Neumann-to-Dirichlet-operator  $\Lambda(\gamma_\omega)$  satisfies

$$\begin{aligned} \int_{\partial\Omega} \bar{g}\Lambda(\gamma_\omega)h \, ds &= \int_{\partial\Omega} \bar{g}u_{\gamma_\omega}^{(h)}|_{\partial\Omega} \, ds = \int_{\Omega} \overline{\gamma_\omega \nabla u_{\gamma_\omega}^{(g)}} \cdot \nabla u_{\gamma_\omega}^{(h)}, \\ \int_{\partial\Omega} g\Lambda(\gamma_\omega)h \, ds &= \int_{\Omega} \gamma_\omega \nabla u_{\gamma_\omega}^{(g)} \cdot \nabla u_{\gamma_\omega}^{(h)} = \int_{\partial\Omega} h\Lambda(\gamma_\omega)g \, ds. \end{aligned}$$

In that sense,  $\Lambda(\gamma_\omega)$  is symmetric but generally (for complex  $\gamma_\omega$ ) not self-adjoint.

In simple two-point conductivity measurement setups, there exists an obvious monotonicity relation. Given a larger conductivity we will require less voltage to drive the same current. Remarkably, this monotonicity relation extends to the case of continuous boundary measurements. For real-valued conductivity functions  $\sigma_1, \sigma_2 \in L_+^\infty(\Omega; \mathbb{R})$  we have that, for all  $g \in L_\diamond^2(\partial\Omega)$ ,

$$\begin{aligned} &\int_{\Omega} \frac{\sigma_2}{\sigma_1}(\sigma_1 - \sigma_2) |\nabla u_{\sigma_2}^{(g)}|^2 \, dx \\ &\leq \int_{\partial\Omega} g(\Lambda(\sigma_2) - \Lambda(\sigma_1))g \, ds \leq \int_{\Omega} (\sigma_1 - \sigma_2) |\nabla u_{\sigma_2}^{(g)}|^2 \, dx, \end{aligned} \tag{2}$$

where  $u_{\sigma_2}^{(g)}$  solves the EIT equation (1) with conductivity  $\sigma_2$  and boundary currents  $g$ . Hence,

$$\sigma_1 \leq \sigma_2 \quad \text{implies that} \quad \Lambda(\sigma_1) \geq \Lambda(\sigma_2),$$

so that an imaging domain with larger conductivity yields to smaller measurements in the sense of operator definiteness. The monotonicity relation (2) goes back to Ikehata, Kang, Seo, and Sheen [53, 46]. It is the basis of many results on inclusion detection in EIT, cf. [54, 45, 34, 35, 36, 38, 33].

The following lemma extends the relation (2) to complex-valued conductivities (see also [54, 34, 36] for similar results).

**Lemma 2.1.** *Let  $\gamma_1, \gamma_2 \in L_+^\infty(\Omega; \mathbb{R}) + iL^\infty(\Omega; \mathbb{R})$ ,  $g \in L_\diamond^2(\partial\Omega)$ , and  $u_{\gamma_1}^{(g)}, u_{\gamma_2}^{(g)} \in H_\diamond^1(\Omega)$  be the corresponding solutions of (1). Then*

$$\begin{aligned} &\int_{\Omega} \left( \frac{\Re(\gamma_2)}{\Re(\gamma_1)} \Re(\gamma_1 - \gamma_2) - \frac{\Im(\gamma_2)^2}{\Re(\gamma_1)} \right) |\nabla u_{\gamma_2}^{(g)}|^2 \, dx \\ &\leq \int_{\partial\Omega} \bar{g} \Re[\Lambda(\gamma_2) - \Lambda(\gamma_1)]g \, ds \leq \int_{\Omega} \left( \Re(\gamma_1 - \gamma_2) + \frac{\Im(\gamma_1)^2}{\Re(\gamma_1)} \right) |\nabla u_{\gamma_2}^{(g)}|^2 \, dx. \end{aligned}$$

The proof of lemma 2.1 is postponed to the end of this section.

### 2.3. Detecting inclusions in the continuous case

We assume that the imaging domain  $\Omega$  consists of a homogeneous background medium with one or several conductivity anomalies (inclusions)  $D$ . For simplicity, we will present our result for the case that the anomalies possess a constant admittivity and that the conductivity  $\sigma_\omega$  and the permittivity  $\epsilon_\omega$  do not change with frequency. More precisely, we assume that  $D \subset \Omega$  is a closed set with connected complement and that  $\gamma_0$  and  $\gamma_\omega$  are given by

$$\gamma_0(x) = \begin{cases} \gamma_0^{(\Omega)} = \sigma_\Omega & \text{for } x \in \Omega \setminus D \\ \gamma_0^{(D)} = \sigma_D & \text{for } x \in D \end{cases} \quad (3)$$

$$\gamma_\omega(x) = \begin{cases} \gamma_\omega^{(\Omega)} = \sigma_\Omega + i\omega\epsilon_\Omega & \text{for } x \in \Omega \setminus D \\ \gamma_\omega^{(D)} = \sigma_D + i\omega\epsilon_D & \text{for } x \in D \end{cases} \quad (4)$$

with real-valued constants  $\sigma_\Omega, \sigma_D, \epsilon_\Omega, \epsilon_D > 0$ . We also assume that the anomaly fulfills

$$\epsilon_D\sigma_\Omega - \epsilon_\Omega\sigma_D \neq 0, \quad (5)$$

which is the contrast condition required to detect inclusion in weighted fdEIT, cf. [34, Remark 2.3]. Our results can easily be extended to inclusions of spatially varying and frequency-dependent admittivities as long as the background conductivities are constant.

The ratio of the background conductivities is denoted by

$$\alpha := \frac{\gamma_\omega^{(\Omega)}}{\gamma_0^{(\Omega)}} = 1 + i\omega \frac{\epsilon_\Omega}{\sigma_\Omega}. \quad (6)$$

Obviously,  $\alpha\Lambda(\gamma_\omega) = \Lambda(\gamma_\omega/\alpha)$ .

We show that the anomaly  $D$  can be detected from comparing (ratio-weighted) EIT measurements at a non-zero frequency  $\omega > 0$  with ultrasound-modulated DC measurements, i.e. that we can detect  $D$  from knowledge of  $\Lambda(\gamma_\omega)$ ,  $\Lambda(\gamma_0(1 + \beta\chi_B))$ , and the background ratio  $\alpha$ . (Note that, the background ratio  $\alpha$  could also be estimated by additionally taking unmodulated DC measurements  $\Lambda(\gamma_0)$  and comparing them with  $\Lambda(\gamma_\omega)$  in the same way as in weighted fdEIT, cf. [69, 34, 36].)

**Theorem 2.2.** *Let  $c := \epsilon_D\sigma_\Omega - \epsilon_\Omega\sigma_D \neq 0$ .*

(a) *If  $c > 0$ , then for sufficiently small  $\beta > 0$  and every open set  $B \subseteq \Omega$ ,*

$$B \subseteq D \quad \text{if and only if} \quad \Re(\alpha\Lambda(\gamma_\omega)) \leq \Lambda((1 + \beta\chi_B)\gamma_0). \quad (7)$$

(b) *If  $c < 0$ , then for sufficiently small  $\beta > 0$  and every open set  $B \subseteq \Omega$ ,*

$$B \subseteq D \quad \text{if and only if} \quad \Re(\alpha\Lambda(\gamma_\omega)) \geq \Lambda((1 - \beta\chi_B)\gamma_0). \quad (8)$$

*The modulation strength  $\beta > 0$  is sufficiently small if*

$$\beta \leq \begin{cases} \omega^2 |c| \frac{\epsilon_\Omega}{\sigma_D(\sigma_\Omega^2 + \omega^2\epsilon_\Omega^2)} & \text{in case (a),} \\ \omega^2 |c| \frac{\epsilon_D}{\sigma_D(\sigma_D\sigma_\Omega + \omega^2\epsilon_D\epsilon_\Omega)} & \text{in case (b).} \end{cases}$$

Theorem 2.2 shows that, for sufficiently small modulation strengths, the ultrasound-modulated DC measurements are larger ( $c > 0$ ), resp., smaller ( $c < 0$ ) than (the self-adjoint part of ratio-weighted) measurements taken at a non-zero frequency if and only if the focusing region lies inside the unknown inclusion  $D$ . The terms larger and smaller are to be understood in the sense of operator definiteness.

**Remark 2.3.** *The monotonicity tests in 2.2 are stable in the following sense (cf. [38, remark 3.5]). Let  $A^\delta$  be a (w.l.o.g. self-adjoint) approximation to the compact and self-adjoint operator  $A$ ,*

$$\|A^\delta - A\|_{\mathcal{L}(L^2_\diamond(\partial\Omega))} < \delta,$$

where  $A := \Lambda((1 + \beta\chi_B)\gamma_0) - \Re(\alpha\Lambda(\gamma_\omega))$  in case (a) of theorem 2.2 and  $A := \Re(\alpha\Lambda(\gamma_\omega)) - \Lambda((1 - \beta\chi_B)\gamma_0)$  in case (b).

We consider the regularized definiteness test

$$A^\delta \geq -\delta I. \quad (9)$$

If  $A \geq 0$ , then  $A^\delta \geq -\delta I$  will be fulfilled. On the other hand, if  $A \not\geq 0$ , then  $A$  must possess a negative eigenvalue  $\lambda < 0$ , so that  $A^\delta \not\geq -\delta I$  for all  $\delta < -\frac{\lambda}{2}$ .

Hence, in order to determine whether a given focusing region lies inside the unknown inclusion, it suffices to know the measurements up to a certain precision level  $\delta > 0$ . In that sense, also our arguably idealistic modeling of a perfectly focused ultrasound beam only has to be approximately valid.

#### 2.4. Proof of lemma 2.1 and theorem 2.2

Our proof of theorem 2.2 relies on the monotonicity relation for complex conductivity EIT in lemma 2.1 and the concept of localized potentials developed by one of the authors in [23]. To prove lemma 2.1, we will first show the following auxiliary result that will also be useful for the case of electrode measurements.

**Lemma 2.4.** *Let  $\gamma_1, \gamma_2 \in L^\infty_+(\Omega; \mathbb{R}) + iL^\infty(\Omega; \mathbb{R})$ ,  $g \in L^2_\diamond(\partial\Omega)$ , and  $u_1, u_2 \in H^1(\Omega)$  fulfill*

$$\begin{aligned} \int_\Omega \gamma_1 |\nabla u_1|^2 \, dx &= \int_\Omega \gamma_2 \nabla u_2 \cdot \overline{\nabla u_1} \, dx, \\ \int_\Omega \gamma_2 |\nabla u_2|^2 \, dx &= \int_\Omega \gamma_1 \nabla u_1 \cdot \overline{\nabla u_2} \, dx. \end{aligned}$$

Then

$$\begin{aligned} &\int_\Omega \left( \frac{\Re(\gamma_2)}{\Re(\gamma_1)} \Re(\gamma_1 - \gamma_2) - \frac{\Im(\gamma_2)^2}{\Re(\gamma_1)} \right) |\nabla u_2|^2 \, dx \\ &\leq \int_\Omega \Re(\gamma_2) |\nabla u_2|^2 \, dx - \int_\Omega \Re(\gamma_1) |\nabla u_1|^2 \, dx \\ &\leq \int_\Omega \left( \Re(\gamma_1 - \gamma_2) + \frac{\Im(\gamma_1)^2}{\Re(\gamma_1)} \right) |\nabla u_2|^2 \, dx. \end{aligned}$$

*Proof.* Since

$$\begin{aligned}
0 &\leq \int_{\Omega} \Re(\gamma_1) \left| \nabla u_1 - \frac{\gamma_2}{\Re(\gamma_1)} \nabla u_2 \right|^2 \\
&= \Re \left( \int_{\Omega} \gamma_1 |\nabla u_1|^2 \, dx - 2 \int_{\Omega} \gamma_2 \nabla u_2 \cdot \overline{\nabla u_1} \, dx \right) + \int_{\Omega} \frac{|\gamma_2|^2}{\Re(\gamma_1)} |\nabla u_2|^2 \, dx \\
&= - \int_{\Omega} \Re(\gamma_1) |\nabla u_1|^2 \, dx + \int_{\Omega} \frac{|\gamma_2|^2}{\Re(\gamma_1)} |\nabla u_2|^2 \, dx \\
&= \int_{\Omega} \Re(\gamma_2) |\nabla u_2|^2 \, dx - \int_{\Omega} \Re(\gamma_1) |\nabla u_1|^2 \, dx + \int_{\Omega} \left( \frac{|\gamma_2|^2}{\Re(\gamma_1)} - \Re(\gamma_2) \right) |\nabla u_2|^2 \, dx,
\end{aligned}$$

the first inequality follows from

$$\frac{|\gamma_2|^2}{\Re(\gamma_1)} - \Re(\gamma_2) = \frac{\Re(\gamma_2)^2 + \Im(\gamma_2)^2}{\Re(\gamma_1)} - \Re(\gamma_2) = \frac{\Re(\gamma_2)}{\Re(\gamma_1)} \Re(\gamma_2 - \gamma_1) + \frac{\Im(\gamma_2)^2}{\Re(\gamma_1)}.$$

Likewise we obtain

$$\begin{aligned}
0 &\leq \int_{\Omega} \Re(\gamma_1) \left| \nabla u_1 - \frac{\overline{\gamma_1}}{\Re(\gamma_1)} \nabla u_2 \right|^2 \\
&= \int_{\Omega} \Re(\gamma_1) |\nabla u_1|^2 \, dx - 2\Re \left( \int_{\Omega} \overline{\gamma_1} \nabla u_2 \cdot \overline{\nabla u_1} \, dx \right) + \int_{\Omega} \frac{|\gamma_1|^2}{\Re(\gamma_1)} |\nabla u_2|^2 \, dx \\
&= \int_{\Omega} \Re(\gamma_1) |\nabla u_1|^2 \, dx - \int_{\Omega} \Re(\gamma_2) |\nabla u_2|^2 \, dx + \int_{\Omega} \left( \frac{|\gamma_1|^2}{\Re(\gamma_1)} - \Re(\gamma_2) \right) |\nabla u_2|^2 \, dx,
\end{aligned}$$

so that the second inequality follows from

$$\frac{|\gamma_1|^2}{\Re(\gamma_1)} - \Re(\gamma_2) = \frac{\Re(\gamma_1)^2 + \Im(\gamma_1)^2}{\Re(\gamma_1)} - \Re(\gamma_2) = \Re(\gamma_1 - \gamma_2) + \frac{\Im(\gamma_1)^2}{\Re(\gamma_1)}.$$

□

We also require the following elementary computation:

**Lemma 2.5.** *Let  $\gamma_0, \gamma_\omega : \Omega \rightarrow \mathbb{C}$ , and  $\alpha \in \mathbb{C}$  be given by (3), (4), and (6). Then, for all  $\tilde{\beta} \in \mathbb{R}$ ,*

$$\begin{aligned}
\frac{\Re(\gamma_0)}{\Re(\gamma_\omega/\alpha)} \Re(\gamma_\omega/\alpha - \gamma_0) &= \begin{cases} 0 & \text{in } \Omega \setminus D, \\ \frac{\epsilon_\Omega \sigma_D}{\sigma_\Omega} C & \text{in } D, \end{cases} \\
\Re(\gamma_\omega/\alpha - \gamma_0) + \frac{\Im(\gamma_\omega/\alpha)^2}{\Re(\gamma_\omega/\alpha)} &= \begin{cases} 0 & \text{in } \Omega \setminus D, \\ \epsilon_D C & \text{in } D, \end{cases} \\
\Re(\gamma_\omega/\alpha - (1 + \tilde{\beta}\chi_B)\gamma_0) &= \begin{cases} -\tilde{\beta}\sigma_\Omega \chi_B & \text{in } \Omega \setminus D, \\ \sigma_D \left( \frac{\epsilon_\Omega}{\sigma_\Omega} C' - \tilde{\beta}\chi_B \right) & \text{in } D, \end{cases} \\
\Re(\gamma_\omega/\alpha - (1 + \tilde{\beta}\chi_B)\gamma_0) + \frac{\Im(\gamma_\omega/\alpha)^2}{\Re(\gamma_\omega/\alpha)} &= \begin{cases} -\tilde{\beta}\sigma_\Omega \chi_B & \text{in } \Omega \setminus D, \\ \epsilon_D C - \tilde{\beta}\sigma_D \chi_B & \text{in } D, \end{cases}
\end{aligned}$$

where

$$C := \omega^2 \frac{\epsilon_D \sigma_\Omega - \epsilon_\Omega \sigma_D}{\sigma_D \sigma_\Omega + \omega^2 \epsilon_D \epsilon_\Omega} \quad \text{and} \quad C' := \omega^2 \frac{\sigma_\Omega}{\sigma_D} \cdot \frac{\epsilon_D \sigma_\Omega - \epsilon_\Omega \sigma_D}{\sigma_\Omega^2 + \omega^2 \epsilon_\Omega^2}. \quad (10)$$

*Proof.* Let

$$\gamma_0 = \begin{cases} \gamma_0^{(\Omega)} = \sigma_\Omega & \text{in } \Omega \setminus D, \\ \gamma_0^{(D)} = \sigma_D & \text{in } D, \end{cases} \quad \gamma_\omega = \begin{cases} \gamma_\omega^{(\Omega)} = \sigma_\Omega + i\omega\epsilon_\Omega & \text{in } \Omega \setminus D, \\ \gamma_\omega^{(D)} = \sigma_D + i\omega\epsilon_D & \text{in } D, \end{cases}$$

with real-valued constants  $\sigma_\Omega, \sigma_D, \epsilon_\Omega, \epsilon_D > 0$ , and let  $\alpha := \gamma_\omega^{(\Omega)}/\gamma_0^{(\Omega)} = 1 + i\omega\frac{\epsilon_\Omega}{\sigma_\Omega} \in \mathbb{C}$ .

Then, by definition of  $\alpha$ ,

$$\gamma_\omega/\alpha - \gamma_0 = 0 \quad \text{in } \Omega \setminus D, \quad \text{and} \quad \Im(\gamma_\omega/\alpha) = 0 \quad \text{in } \Omega \setminus D,$$

so that

$$\begin{aligned} \frac{\Re(\gamma_0)}{\Re(\gamma_\omega/\alpha)} \Re(\gamma_\omega/\alpha - \gamma_0) &= 0 \quad \text{in } \Omega \setminus D, \\ \Re(\gamma_\omega/\alpha - \gamma_0) + \frac{\Im(\gamma_\omega/\alpha)^2}{\Re(\gamma_\omega/\alpha)} &= 0 \quad \text{in } \Omega \setminus D, \\ \Re(\gamma_\omega/\alpha - (1 + \tilde{\beta}\chi_B)\gamma_0) &= -\tilde{\beta}\sigma_\Omega\chi_B \quad \text{in } \Omega \setminus D, \\ \Re(\gamma_\omega/\alpha - (1 + \tilde{\beta}\chi_B)\gamma_0) + \frac{\Im(\gamma_\omega/\alpha)^2}{\Re(\gamma_\omega/\alpha)} &= -\tilde{\beta}\sigma_\Omega\chi_B \quad \text{in } \Omega \setminus D. \end{aligned}$$

In  $D$ , we have that

$$\begin{aligned} \Re(\gamma_0) &= \sigma_D, \\ \Re(\gamma_\omega/\alpha) &= \Re\left(\gamma_\omega^{(D)} \frac{\gamma_0^{(\Omega)}}{\gamma_\omega^{(\Omega)}}\right) = \sigma_\Omega \Re\left(\frac{\sigma_D + i\omega\epsilon_D}{\sigma_\Omega + i\omega\epsilon_\Omega}\right) = \sigma_\Omega \frac{\sigma_D\sigma_\Omega + \omega^2\epsilon_D\epsilon_\Omega}{\sigma_\Omega^2 + \omega^2\epsilon_\Omega^2}, \\ \Im(\gamma_\omega/\alpha) &= \Im\left(\gamma_\omega^{(D)} \frac{\gamma_0^{(\Omega)}}{\gamma_\omega^{(\Omega)}}\right) = \sigma_\Omega \Im\left(\frac{\sigma_D + i\omega\epsilon_D}{\sigma_\Omega + i\omega\epsilon_\Omega}\right) = \omega\sigma_\Omega \frac{\epsilon_D\sigma_\Omega - \epsilon_\Omega\sigma_D}{\sigma_\Omega^2 + \omega^2\epsilon_\Omega^2}. \end{aligned}$$

Hence, in  $D$ ,

$$\Re(\gamma_\omega/\alpha - \gamma_0) = \sigma_\Omega \frac{\sigma_D\sigma_\Omega + \omega^2\epsilon_D\epsilon_\Omega}{\sigma_\Omega^2 + \omega^2\epsilon_\Omega^2} - \sigma_D = \omega^2\epsilon_\Omega \frac{\epsilon_D\sigma_\Omega - \sigma_D\epsilon_\Omega}{\sigma_\Omega^2 + \omega^2\epsilon_\Omega^2} = \frac{\epsilon_\Omega\sigma_D}{\sigma_\Omega} C',$$

which shows that

$$\frac{\Re(\gamma_0)}{\Re(\gamma_\omega/\alpha)} \Re(\gamma_\omega/\alpha - \gamma_0) = \omega^2\sigma_D\epsilon_\Omega \frac{\epsilon_D\sigma_\Omega - \epsilon_\Omega\sigma_D}{\sigma_\Omega(\sigma_D\sigma_\Omega + \omega^2\epsilon_D\epsilon_\Omega)} = \frac{\epsilon_\Omega\sigma_D}{\sigma_\Omega} C,$$

and

$$\Re(\gamma_\omega/\alpha - (1 + \tilde{\beta}\chi_B)\gamma_0) = \sigma_D \left( \frac{\epsilon_\Omega}{\sigma_\Omega} C' - \tilde{\beta}\chi_B \right).$$

The remaining two equalities follow from

$$\begin{aligned} \Re(\gamma_\omega/\alpha - \gamma_0) + \frac{\Im(\gamma_\omega/\alpha)^2}{\Re(\gamma_\omega/\alpha)} &= \omega^2\epsilon_\Omega \frac{\epsilon_D\sigma_\Omega - \epsilon_\Omega\sigma_D}{\sigma_\Omega^2 + \omega^2\epsilon_\Omega^2} + \omega^2\sigma_\Omega \frac{(\epsilon_D\sigma_\Omega - \epsilon_\Omega\sigma_D)^2}{(\sigma_\Omega^2 + \omega^2\epsilon_\Omega^2)(\sigma_D\sigma_\Omega + \omega^2\epsilon_D\epsilon_\Omega)} \\ &= \omega^2 \frac{\epsilon_D\sigma_\Omega - \epsilon_\Omega\sigma_D}{\sigma_\Omega^2 + \omega^2\epsilon_\Omega^2} \left( \epsilon_\Omega + \sigma_\Omega \frac{\epsilon_D\sigma_\Omega - \epsilon_\Omega\sigma_D}{\sigma_D\sigma_\Omega + \omega^2\epsilon_D\epsilon_\Omega} \right) \end{aligned}$$

$$= \omega^2 \frac{\epsilon_D \sigma_\Omega - \epsilon_\Omega \sigma_D}{\sigma_\Omega^2 + \omega^2 \epsilon_\Omega^2} \frac{\omega^2 \epsilon_D \epsilon_\Omega^2 + \epsilon_D \sigma_\Omega^2}{\sigma_D \sigma_\Omega + \omega^2 \epsilon_D \epsilon_\Omega} = \omega^2 \epsilon_D \frac{\epsilon_D \sigma_\Omega - \epsilon_\Omega \sigma_D}{\sigma_D \sigma_\Omega + \omega^2 \epsilon_D \epsilon_\Omega} = \epsilon_D C,$$

which also yields

$$\Re(\gamma_\omega/\alpha - (1 + \tilde{\beta}\chi_B)\gamma_0) + \frac{\Im(\gamma_\omega/\alpha)^2}{\Re(\gamma_\omega/\alpha)} = \epsilon_D C - \tilde{\beta}\sigma_D \chi_B.$$

□

Now we are ready to prove lemma 2.1 and theorem 2.2.

*Proof of lemma 2.1.* For all  $g \in L_\diamond^2(\partial\Omega)$  we have that

$$\begin{aligned} \int_{\partial\Omega} \bar{g} \Lambda(\gamma_1) g \, ds &= \int_{\partial\Omega} \bar{g} u_{\gamma_1}^{(g)}|_{\partial\Omega} \, ds = \int_{\Omega} \overline{\gamma_1} |\nabla u_{\gamma_1}^{(g)}|^2 \, dx = \int_{\Omega} \overline{\gamma_2 \nabla u_{\gamma_2}^{(g)}} \cdot \nabla u_{\gamma_1}^{(g)} \, dx, \\ \int_{\partial\Omega} \bar{g} \Lambda(\gamma_2) g \, ds &= \int_{\partial\Omega} \bar{g} u_{\gamma_2}^{(g)}|_{\partial\Omega} \, ds = \int_{\Omega} \overline{\gamma_2} |\nabla u_{\gamma_2}^{(g)}|^2 \, dx = \int_{\Omega} \overline{\gamma_1 \nabla u_{\gamma_1}^{(g)}} \cdot \nabla u_{\gamma_2}^{(g)} \, dx, \end{aligned}$$

so that the assertion of lemma 2.1 immediately follows from lemma 2.4. □

*Proof of theorem 2.2.*

- (a) (i) Let  $c := \epsilon_D \sigma_\Omega - \epsilon_\Omega \sigma_D > 0$ , and  $B \subseteq D$ .

We use the first inequality in lemma 2.1 with  $\gamma_2 := (1 + \beta\chi_B)\gamma_0$ , and  $\gamma_1 := \gamma_\omega/\alpha$  together with the third equality in lemma 2.5 with  $\tilde{\beta} := \beta$  to obtain that, for all  $g \in L_\diamond^2(\partial\Omega)$ ,

$$\begin{aligned} &\int_{\partial\Omega} \bar{g} [\Lambda((1 + \beta\chi_B)\gamma_0) - \Re(\Lambda(\gamma_\omega/\alpha))] g \, ds \\ &\geq \int_{\Omega} \frac{\Re((1 + \beta\chi_B)\gamma_0)}{\Re(\gamma_\omega/\alpha)} \Re(\gamma_\omega/\alpha - (1 + \beta\chi_B)\gamma_0) |\nabla u_{\gamma_2}^{(g)}|^2 \, dx \\ &= \int_D \frac{(1 + \beta\chi_B)\gamma_0}{\Re(\gamma_\omega/\alpha)} \sigma_D \left( \frac{\epsilon_\Omega}{\sigma_\Omega} C' - \beta\chi_B \right) |\nabla u_{\gamma_2}^{(g)}|^2 \, dx, \end{aligned}$$

where  $C'$  is defined by (10) in lemma 2.5. The right hand side is non-negative if

$$\beta \leq \frac{\epsilon_\Omega}{\sigma_\Omega} C' = \omega^2 |c| \frac{\epsilon_\Omega}{\sigma_D (\sigma_\Omega^2 + \omega^2 \epsilon_\Omega^2)},$$

so that, for sufficiently small  $\beta > 0$ ,

$$B \subseteq D \quad \text{implies} \quad \Re(\alpha \Lambda(\gamma_\omega)) \leq \Lambda((1 + \beta\chi_B)\gamma_0).$$

- (ii) Now let  $c := \epsilon_D \sigma_\Omega - \epsilon_\Omega \sigma_D > 0$ , and  $B \not\subseteq D$ .

We use the second inequality in lemma 2.1 with  $\gamma_2 := \gamma_0$ , and  $\gamma_1 := \gamma_\omega/\alpha$  together with the second equality in lemma 2.5 to obtain that, for all  $g \in L_\diamond^2(\partial\Omega)$ ,

$$\begin{aligned} &\int_{\partial\Omega} \bar{g} [\Lambda(\gamma_0) - \Re(\Lambda(\gamma_\omega/\alpha))] g \, ds \\ &\leq \int_{\Omega} \left( \Re(\gamma_\omega/\alpha - \gamma_0) + \frac{\Im(\gamma_\omega/\alpha)^2}{\Re(\gamma_\omega/\alpha)} \right) |\nabla u_{\gamma_0}^{(g)}|^2 \, dx \\ &= \epsilon_D C \int_D |\nabla u_{\gamma_0}^{(g)}|^2 \, dx, \end{aligned}$$

where  $C$  is defined by (10) in lemma 2.5. The first inequality in lemma 2.1 with  $\gamma_2 := \gamma_0$  and  $\gamma_1 := (1 + \beta\chi_B)\gamma_0$  yields that, for all  $g \in L_\diamond^2(\partial\Omega)$ ,

$$\int_B \frac{\beta}{1 + \beta} \gamma_0 |\nabla u_{\gamma_0}^{(g)}|^2 dx \leq \int_{\partial\Omega} \bar{g} [\Lambda(\gamma_0) - \Lambda((1 + \beta\chi_B)\gamma_0)] g ds.$$

Combining both inequalities, we obtain that, for all  $g \in L_\diamond^2(\partial\Omega)$ ,

$$\begin{aligned} & \int_{\partial\Omega} \bar{g} [\Lambda((1 + \beta\chi_B)\gamma_0) - \Re(\alpha\Lambda(\gamma_\omega))] g ds \\ & \leq \epsilon_D C \int_D |\nabla u_{\gamma_0}^{(g)}|^2 dx - \int_B \frac{\beta}{1 + \beta} \gamma_0 |\nabla u_{\gamma_0}^{(g)}|^2 dx. \end{aligned}$$

Now we apply the technique of localized potentials [23, 38] to show that the right hand side of this inequality attains negative values. Since  $B \not\subseteq D$  we can choose a smaller open subset  $B' \subseteq B$  with  $\overline{B'} \cap D = \emptyset$ . Since  $D \subset \Omega$  and  $\Omega \setminus D$  is connected, we obtain from [38, Thm. 3.6] a sequence of currents  $(g_k)_{k \in \mathbb{N}} \subset L_\diamond^2(\partial\Omega)$ , so that the solutions  $(u^{(g_k)})_{k \in \mathbb{N}} \subset H_\diamond^1(\Omega)$  of

$$\Delta u^{(g_k)} = 0, \quad \partial_\nu u^{(g_k)}|_{\partial\Omega} = g_k$$

fulfill

$$\lim_{k \rightarrow \infty} \int_{B'} |\nabla u^{(g_k)}|^2 dx = \infty \quad \text{and} \quad \lim_{k \rightarrow \infty} \int_D |\nabla u^{(g_k)}|^2 dx = 0.$$

Since  $\gamma_0$  is constant on  $\Omega \setminus D$ , [38, Lemma 3.7] yields that also the corresponding solutions  $(u_{\gamma_0}^{(g_k)})_{k \in \mathbb{N}} \subset H_\diamond^1(\Omega)$  of (1) fulfill

$$\lim_{k \rightarrow \infty} \int_{B'} |\nabla u_{\gamma_0}^{(g_k)}|^2 dx = \infty \quad \text{and} \quad \lim_{k \rightarrow \infty} \int_D |\nabla u_{\gamma_0}^{(g_k)}|^2 dx = 0.$$

Hence, with this sequence of currents,

$$\int_{\partial\Omega} \bar{g}_k [\Lambda((1 + \beta\chi_B)\gamma_0) - \Re(\alpha\Lambda(\gamma_\omega))] g_k ds \rightarrow -\infty,$$

which shows that, for all  $\beta > 0$ ,

$$B \not\subseteq D \quad \text{implies} \quad \Re(\alpha\Lambda(\gamma_\omega)) \not\leq \Lambda((1 + \beta\chi_B)\gamma_0).$$

- (b) (i) Let  $c := \epsilon_D \sigma_\Omega - \epsilon_\Omega \sigma_D < 0$ , and  $B \subseteq D$ .

We use the second inequality in lemma 2.1 with  $\gamma_2 := (1 - \beta\chi_B)\gamma_0$ , and  $\gamma_1 := \gamma_\omega/\alpha$  together with the fourth equality in lemma 2.5 with  $\tilde{\beta} := -\beta$  to obtain that, for all  $g \in L_\diamond^2(\partial\Omega)$ ,

$$\begin{aligned} & \int_{\partial\Omega} \bar{g} [\Lambda((1 - \beta\chi_B)\gamma_0) - \Re(\alpha\Lambda(\gamma_\omega))] g ds \\ & \leq \int_\Omega \left( \Re(\gamma_\omega/\alpha - (1 - \beta\chi_B)\gamma_0) + \frac{\Im(\gamma_\omega/\alpha)^2}{\Re(\gamma_\omega/\alpha)} \right) |\nabla u_{\gamma_2}^{(g)}|^2 dx \\ & = \int_D (\epsilon_D C + \beta \sigma_D \chi_B) |\nabla u_{\gamma_2}^{(g)}|^2 dx. \end{aligned}$$

The right hand side is non-positive if

$$\beta \leq -\frac{\epsilon_D}{\sigma_D} C = \omega^2 |c| \frac{\epsilon_D}{\sigma_D (\sigma_D \sigma_\Omega + \omega^2 \epsilon_D \epsilon_\Omega)},$$

so that, for sufficiently small  $\beta > 0$ ,

$$B \subseteq D \quad \text{implies} \quad \Re(\alpha\Lambda(\gamma_\omega)) \geq \Lambda((1 - \beta\chi_B)\gamma_0).$$

(ii) Now let  $c := \epsilon_D \sigma_\Omega - \epsilon_\Omega \sigma_D < 0$ , and  $B \not\subseteq D$ .

We use the first inequality in lemma 2.1 with  $\gamma_2 := \gamma_0$ , and  $\gamma_1 := \gamma_\omega/\alpha$  together with the first equality in lemma 2.5 to obtain that, for all  $g \in L^2_\diamond(\partial\Omega)$ ,

$$\begin{aligned} & \int_{\partial\Omega} \bar{g} [\Lambda(\gamma_0) - \Re(\Lambda(\gamma_\omega/\alpha))] g \, ds \\ & \geq \int_\Omega \frac{\Re(\gamma_0)}{\Re(\gamma_\omega/\alpha)} \Re(\gamma_\omega/\alpha - \gamma_0) |\nabla u_{\gamma_0}^{(g)}|^2 \, dx \\ & = \frac{\epsilon_\Omega \sigma_D}{\sigma_\Omega} C \int_D |\nabla u_{\gamma_0}^{(g)}|^2 \, dx. \end{aligned}$$

The second inequality in lemma 2.1 with  $\gamma_2 := \gamma_0$  and  $\gamma_1 := (1 - \beta\chi_B)\gamma_0$  yields that, for all  $g \in L^2_\diamond(\partial\Omega)$ ,

$$\int_{\partial\Omega} \bar{g} [\Lambda(\gamma_0) - \Lambda((1 - \beta\chi_B)\gamma_0)] g \, ds \leq - \int_B \beta\gamma_0 |\nabla u_{\gamma_0}^{(g)}|^2 \, dx.$$

Combining both inequalities, we obtain that, for all  $g \in L^2_\diamond(\partial\Omega)$ ,

$$\begin{aligned} & \int_{\partial\Omega} \bar{g} [\Lambda((1 - \beta\chi_B)\gamma_0) - \Re(\alpha\Lambda(\gamma_\omega))] g \, ds \\ & \geq \frac{\epsilon_\Omega \sigma_D}{\sigma_\Omega} C \int_D |\nabla u_{\gamma_0}^{(g)}|^2 \, dx + \int_B \beta\gamma_0 |\nabla u_{\gamma_0}^{(g)}|^2 \, dx. \end{aligned}$$

The same localized potentials argument as in part (a)(ii) shows that there exists a sequence of currents such that

$$\int_{\partial\Omega} \bar{g} [\Lambda((1 - \beta\chi_B)\gamma_0) - \Re(\alpha\Lambda(\gamma_\omega))] g \, ds \rightarrow \infty.$$

Hence, for all  $\beta > 0$ ,

$$B \not\subseteq D \quad \text{implies} \quad \Re(\alpha\Lambda(\gamma_\omega)) \not\geq \Lambda((1 - \beta\chi_B)\gamma_0).$$

□

### 3. Electrode measurements

#### 3.1. The setting

In a realistic setting, the currents will be applied using a finite number of electrodes  $\mathcal{E}_l \subset \partial\Omega$ ,  $l = 1, \dots, m$ , that are attached to the imaging domain's surface. We assume that the electrodes are perfectly conducting and that contact impedances are negligible (the so-called *shunt model*, cf., e.g., [16]). Driving a current  $I_l \in \mathbb{C}$  through the  $l$ -th electrode, with  $\sum_{l=1}^m I_l = 0$ , the electric potential is given by the solution  $u_{\gamma_\omega} \in H^1_{\mathcal{E}}(\Omega)$  of

$$\nabla \cdot (\gamma_\omega \nabla u_{\gamma_\omega}) = 0 \quad \text{in } \Omega, \tag{11}$$

$$\int_{\mathcal{E}_l} \gamma_\omega \partial_\nu u_{\gamma_\omega} \, ds = I_l \quad \text{for } l = 1, \dots, m, \tag{12}$$

$$\gamma_\omega \partial_\nu u_{\gamma_\omega} = 0 \quad \text{on } \partial\Omega \setminus \bigcup_{l=1}^m \mathcal{E}_l, \tag{13}$$

$$u_{\gamma_\omega}|_{\mathcal{E}_l} = \text{const.} \quad \forall j = 1, \dots, m, \tag{14}$$

where  $H_{\mathcal{E}}^1(\Omega)$  is the subspace of  $H^1$ -functions that are locally constant on each  $\mathcal{E}_l$ ,  $l = 1, \dots, m$  and these constants sum up to zero.

We assume that the voltage-current-measurements are carried out in the following complete dipole-dipole configuration. Let  $(j_r, k_r)$ ,  $r = 1, \dots, N$  be a set of electrode pairs with  $j_r \neq k_r$ . For each of these pairs,  $r = 1, \dots, N$ , a current of  $I_{j_r} = 1$  and  $I_{k_r} = -1$  is driven through the  $j_r$ -th and the  $k_r$ -th electrode, respectively. The other electrodes are kept insulated. The resulting electric potential inside the imaging domain is given by the solution  $u_{\gamma_\omega}^{(r)} \in H_{\mathcal{E}}^1(\Omega)$  of (11)–(14) with  $I_l = \delta_{l,j_r} - \delta_{l,k_r}$ ,  $l = 1, \dots, N$ .

While the current is driven through the  $r$ -th pair of electrodes, we measure the required voltage difference on all pairs of electrodes, i.e., between the  $j_s$  and the  $k_s$  electrode for all  $s = 1, \dots, N$ . We collect these measurements in the matrix

$$R(\gamma_\omega) = (u_{\gamma_\omega}^{(r)}|_{\mathcal{E}_{j_s}} - u_{\gamma_\omega}^{(r)}|_{\mathcal{E}_{k_s}})_{r,s=1,\dots,N} \in \mathbb{C}^{N \times N}.$$

Let us comment on our use of the shunt electrode model. It seems to be widely accepted that the most accurate electrode model in EIT is the *complete electrode model*, cf., e.g., [16], where not only the shunting effects but also contact impedances between the electrodes and the imaging domain are taken into account. The effect of contact impedances is often neglected in the case that voltages are not measured on current driven electrodes, but our method requires such measurements, see below. Contact impedances can also be neglected in the case of DC difference measurements on point electrodes, see [29]. Since both, the effect of an ultrasound modulation and the effect of a (weighted) frequency change on the measurements are widely analogous to using DC difference measurements, we believe that our use of the shunt model is justified for sufficiently small electrodes, though this has yet to be justified rigorously.

We also stress that our method relies on the matrix structure of the measurements  $R$ , which means that the same electrode pairs have to be used for measuring voltages and applying currents. In particular, we require voltage measurements on current driven electrodes (for the three main diagonals in  $R$ ). The simultaneous measurement of voltage and current is usually considered problematic and these measurements are avoided in traditional EIT approaches. Nevertheless, successful reconstructions have already been obtained in practical phantom experiments with methods requiring the full matrix such as the factorization method and monotonicity-based methods, cf. [36, 80]. Also, the recent preprint [32] studies the possibility of interpolating the voltages on current-driven electrodes from the measurements on current-free electrodes.

### 3.2. Monotonicity results for the shunt model

As in the continuous case, we will compare measurements in the sense of matrix definiteness. We define the self-adjoint part of a matrix  $A \in \mathbb{C}^{N \times N}$  by setting

$$\Re(A) := \frac{1}{2}(A + A^*)$$

where  $A^* \in \mathbb{C}^{N \times N}$  is the adjoint (conjugate transpose) of  $A$ , i.e.,

$$g^*(Ah) = (Ag)^*h \quad \text{for all } g, h \in \mathbb{C}^N, \quad \text{and} \quad g^* = \bar{g}^T.$$

Obviously,  $\Re(A)$  is self-adjoint.

For two self-adjoint matrices  $A, B \in \mathbb{C}^{N \times N}$ , we write  $A \leq B$  if  $B - A$  is positive semidefinite, i.e.

$$g^*Ag \leq g^*Bg \quad \forall g \in \mathbb{C}^N.$$

This is equivalent to the fact that all eigenvalues of  $B - A$  are non-negative.

Note that the entries of the measurement matrix  $R(\gamma_\omega)$  satisfy

$$\begin{aligned} u_{\gamma_\omega}^{(r)}|_{\mathcal{E}_{js}} - u_{\gamma_\omega}^{(r)}|_{\mathcal{E}_{ks}} &= u_{\gamma_\omega}^{(r)}|_{\mathcal{E}_{js}} \int_{\mathcal{E}_{js}} \gamma_\omega \partial_\nu u_{\gamma_\omega}^{(s)} \, ds + u_{\gamma_\omega}^{(r)}|_{\mathcal{E}_{ks}} \int_{\mathcal{E}_{ks}} \gamma_\omega \partial_\nu u_{\gamma_\omega}^{(s)} \, ds \\ &= \int_{\partial\Omega} \gamma_\omega \partial_\nu u_{\gamma_\omega}^{(s)}|_{\partial\Omega} u_{\gamma_\omega}^{(r)}|_{\partial\Omega} \, ds = \int_{\Omega} \gamma_\omega \nabla u_{\gamma_\omega}^{(r)} \cdot \nabla u_{\gamma_\omega}^{(s)} = u_{\gamma_\omega}^{(s)}|_{\mathcal{E}_{jr}} - u_{\gamma_\omega}^{(s)}|_{\mathcal{E}_{kr}}. \end{aligned}$$

Hence  $R(\gamma_\omega)$  is a symmetric, but generally (for complex  $\gamma_\omega$ ) not self-adjoint matrix. This also shows that the self-adjoint part of the measurement matrix  $\Re(R(\gamma_\omega))$  is identical to the matrix containing the real part of each voltage measurement

$$\Re(R(\gamma_\omega)) = (\Re(u_{\gamma_\omega}^{(r)})|_{\mathcal{E}_{js}} - \Re(u_{\gamma_\omega}^{(r)})|_{\mathcal{E}_{ks}})_{r,s=1,\dots,N} \in \mathbb{R}^{N \times N}.$$

The monotonicity estimate from the continuous case can be extended to the case of electrode measurements.

**Lemma 3.1.** *Let  $\gamma_1, \gamma_2 \in L_+^\infty(\Omega; \mathbb{R}) + iL^\infty(\Omega; \mathbb{R})$ ,  $g = (g_r)_{r=1}^N \in \mathbb{C}^N$  and  $u_{\gamma_\tau}^{[g]} \in H_{\mathcal{E}}^1(\Omega)$  ( $\tau = 1, 2$ ) denote the solution of*

$$\begin{aligned} \nabla \cdot (\gamma_\tau \nabla u_{\gamma_\tau}^{[g]}) &= 0 \quad \text{in } \Omega, \\ \int_{\mathcal{E}_l} \gamma_\tau \partial_\nu u_{\gamma_\tau}^{[g]} \, ds &= \sum_{r: j_r=l} g_r - \sum_{r: k_r=l} g_r \quad \text{for all } l = 1, \dots, m, \\ \gamma_\tau \partial_\nu u_{\gamma_\tau}^{[g]} &= 0 \quad \text{on } \partial\Omega \setminus \bigcup_{l=1}^m \mathcal{E}_l, \\ u_{\gamma_\tau}^{[g]}|_{\mathcal{E}_l} &= \text{const.} \quad \forall l = 1, \dots, m. \end{aligned}$$

Then

$$\begin{aligned} \int_{\Omega} \left( \frac{\Re(\gamma_2)}{\Re(\gamma_1)} \Re(\gamma_1 - \gamma_2) - \frac{\Im(\gamma_2)^2}{\Re(\gamma_1)} \right) |\nabla u_{\gamma_2}^{[g]}|^2 \, dx \\ \leq g^* \Re[R(\gamma_2) - R(\gamma_1)] g \leq \int_{\Omega} \left( \Re(\gamma_1 - \gamma_2) + \frac{\Im(\gamma_1)^2}{\Re(\gamma_1)} \right) |\nabla u_{\gamma_2}^{[g]}|^2 \, dx. \end{aligned}$$

The proof of lemma 3.1 is postponed to the end of this section.

### 3.3. Detecting inclusions from electrode measurements

We make the same assumptions as for the continuous case in subsection 2.3. The inclusion (or anomaly)  $D \subset \Omega$  is assumed to be a closed set with connected complement.  $\gamma_0$  and  $\gamma_\omega$  are assumed to be given by

$$\gamma_0(x) = \begin{cases} \gamma_0^{(\Omega)} = \sigma_\Omega & \text{for } x \in \Omega \\ \gamma_0^{(D)} = \sigma_D & \text{for } x \in D \end{cases}$$

$$\gamma_\omega(x) = \begin{cases} \gamma_\omega^{(\Omega)} = \sigma_\Omega + i\omega\epsilon_\Omega & \text{for } x \in \Omega \\ \gamma_\omega^{(D)} = \sigma_D + i\omega\epsilon_D & \text{for } x \in D \end{cases}$$

with real-valued constants  $\sigma_\Omega, \sigma_D, \epsilon_\Omega, \epsilon_D > 0$ . The anomaly is assumed to fulfill the contrast condition (5), i.e.,  $\epsilon_D\sigma_\Omega - \epsilon_\Omega\sigma_D \neq 0$ , and

$$\alpha := \frac{\gamma_\omega^{(\Omega)}}{\gamma_0^{(\Omega)}} = 1 + i\omega \frac{\epsilon_\Omega}{\sigma_\Omega}.$$

denotes the ratio of the background conductivities. Obviously,  $\alpha R(\gamma_\omega) = R(\gamma_\omega/\alpha)$ .

As in section 2, the results in this section can easily be extended to inclusions of spatially varying and frequency-dependent admittivities as long as the background conductivities are constant.

Our results for continuous boundary data suggest to compare, for sufficiently small modulation strengths  $\beta > 0$ , the matrix of ultrasound-modulated DC measurements  $R((1+\beta\chi_B)\gamma_0)$  with the (self-adjoint part of the ratio-weighted) matrix of measurements taken at a non-zero frequency  $R(\gamma_\omega)$ . This comparison (in the sense of matrix definiteness) should yield information about whether the focusing region  $B$  lies inside the unknown inclusion  $D$ . Indeed, we can prove the following theorem.

**Theorem 3.2.** *Let  $c := \epsilon_D\sigma_\Omega - \epsilon_\Omega\sigma_D \neq 0$ .*

(a) *If  $c > 0$ , then for sufficiently small  $\beta > 0$  and every open set  $B \subseteq \Omega$ ,*

$$B \subseteq D \quad \text{implies that} \quad \Re(\alpha R(\gamma_\omega)) \leq R((1 + \beta\chi_B)\gamma_0). \quad (15)$$

(b) *If  $c < 0$ , then for sufficiently small  $\beta > 0$  and every open set  $B \subseteq \Omega$ ,*

$$B \subseteq D \quad \text{implies that} \quad \Re(\alpha R(\gamma_\omega)) \geq R((1 - \beta\chi_B)\gamma_0). \quad (16)$$

*The modulation strength  $\beta > 0$  is sufficiently small if*

$$\beta \leq \begin{cases} \omega^2 |c| \frac{\epsilon_\Omega}{\sigma_D(\sigma_\Omega^2 + \omega^2 \epsilon_\Omega^2)} & \text{in case (a),} \\ \omega^2 |c| \frac{\epsilon_D}{\sigma_D(\sigma_D \sigma_\Omega + \omega^2 \epsilon_D \epsilon_\Omega)} & \text{in case (b).} \end{cases}$$

The converses of the implications (15) and (16) will generally not be true in the case of measurements with a finite number of electrodes. However, when we increase the number of electrodes used for the measurements, then we can expect that the measurement matrices  $R(\gamma_\omega)$  and  $R((1 + \beta\chi_B)\gamma_0)$  more and more resemble their continuous counterparts, the Neumann-to-Dirichlet operators, cf. the works of Hakula, Hyvönen and Lechleiter [41, 59, 42]. In fact, we can give the following intuitive justification of the converses of the implications in theorem 3.2 for sufficiently many electrodes in the spirit of [36].

**Remark 3.3.** *Let  $B \not\subseteq D$  and  $\beta > 0$ . If there exists a current pattern  $g = (g_r)_{r=1}^N \in \mathbb{C}^N$  such that the resulting DC potential*

$$u_{\gamma_0}^{[g]} := \sum_{r=1}^N g_r u_{\gamma_0}^{\langle r \rangle}$$

possesses a very large energy in  $B \setminus D$  and a very small energy in  $D$ , then

$$\Re(\alpha R(\gamma_\omega)) \leq R((1 + \beta\chi_B)\gamma_0) \quad \text{if } c > 0$$

or

$$\Re(\alpha R(\gamma_\omega)) \geq R((1 - \beta\chi_B)\gamma_0) \quad \text{if } c < 0.$$

### 3.4. Proof of lemma 3.1, theorem 3.2 and justification of remark 3.3

*Proof of lemma 3.1.* Let  $g = (g_r)_{r=1}^N \in \mathbb{C}^N$ . First note that for  $\tau = 1, 2$ , by linearity,

$$u_{\gamma_\tau}^{[g]} = \sum_{r=1}^N u_{\gamma_\tau}^{\langle r \rangle} g_r \quad \text{and} \quad \sum_{r=1}^N g_r (u_{\gamma_\tau}^{\langle r \rangle}|_{\mathcal{E}_{js}} - u_{\gamma_\tau}^{\langle r \rangle}|_{\mathcal{E}_{ks}}) = u_{\gamma_\tau}^{[g]}|_{\mathcal{E}_{js}} - u_{\gamma_\tau}^{[g]}|_{\mathcal{E}_{ks}}.$$

We thus obtain

$$\begin{aligned} g^* R(\gamma_1) g &= \sum_{s=1}^N \overline{g_s} (u_{\gamma_1}^{[g]}|_{\mathcal{E}_{js}} - u_{\gamma_1}^{[g]}|_{\mathcal{E}_{ks}}) = \sum_{l=1}^m \left( \sum_{s: j_s=l} \overline{g_s} - \sum_{s: k_s=l} \overline{g_s} \right) u_{\gamma_1}^{[g]}|_{\mathcal{E}_l} \\ &= \sum_{l=1}^m \int_{\mathcal{E}_l} \overline{\gamma_1 \partial_\nu u_{\gamma_1}^{[g]}}|_{\mathcal{E}_l} u_{\gamma_1}^{[g]}|_{\mathcal{E}_l} \, ds = \int_{\partial\Omega} \overline{\gamma_1 \partial_\nu u_{\gamma_1}^{[g]}} u_{\gamma_1}^{[g]} \, ds = \int_{\Omega} \overline{\gamma_1} |\nabla u_{\gamma_1}^{[g]}|^2 \, dx \\ &= \sum_{l=1}^m \int_{\mathcal{E}_l} \overline{\gamma_2 \partial_\nu u_{\gamma_2}^{[g]}}|_{\mathcal{E}_l} u_{\gamma_1}^{[g]}|_{\mathcal{E}_l} \, ds = \int_{\partial\Omega} \overline{\gamma_2 \partial_\nu u_{\gamma_2}^{[g]}} u_{\gamma_1}^{[g]} \, ds = \int_{\Omega} \overline{\gamma_2 \nabla u_{\gamma_2}^{[g]}} \cdot \nabla u_{\gamma_1}^{[g]} \, dx \end{aligned}$$

and likewise

$$g^* R(\gamma_2) g = \int_{\Omega} \overline{\gamma_2} |\nabla u_{\gamma_2}^{[g]}|^2 \, dx = \int_{\Omega} \overline{\gamma_1 \nabla u_{\gamma_1}^{[g]}} \cdot \nabla u_{\gamma_2}^{[g]} \, dx.$$

Hence, the assertion follows from lemma 2.4.  $\square$

*Proof of theorem 3.2.* The proof is identical to that of theorem 2.2(a)(i) and (b)(i) with lemma 3.1 replacing lemma 2.1.  $\square$

*Justification of remark 3.3.* As in theorem 2.2(a)(ii) and (b)(ii) (with lemma 3.1 replacing lemma 2.1), we obtain that, for all  $g \in \mathbb{C}^N$ ,

$$g^* [R((1 + \beta\chi_B)\gamma_0) - \Re(\alpha R(\gamma_\omega))] g \leq \epsilon_D C \int_D |\nabla u_{\gamma_0}^{[g]}|^2 \, dx - \int_B \frac{\beta}{1 + \beta} \gamma_0 |\nabla u_{\gamma_0}^{[g]}|^2 \, dx.$$

and

$$g^* [R((1 - \beta\chi_B)\gamma_0) - \Re(\alpha R(\gamma_\omega))] g \geq \frac{\epsilon_\Omega \sigma_D}{\sigma_\Omega} C \int_D |\nabla u_{\gamma_0}^{[g]}|^2 \, dx + \int_B \beta \gamma_0 |\nabla u_{\gamma_0}^{[g]}|^2 \, dx$$

where  $C$  is defined by (10) in lemma 2.5.

Hence, if there exists a current pattern  $g = (g_r)_{r=1}^N \in \mathbb{C}^N$  such that the resulting DC potential  $u_{\gamma_0}^{[g]}$  possesses a very large energy in  $B \setminus D$  and a very small energy in  $D$ , then for this  $g$ , we can expect that

$$g^* [R((1 + \beta\chi_B)\gamma_0) - \Re(\alpha R(\gamma_\omega))] g < 0,$$

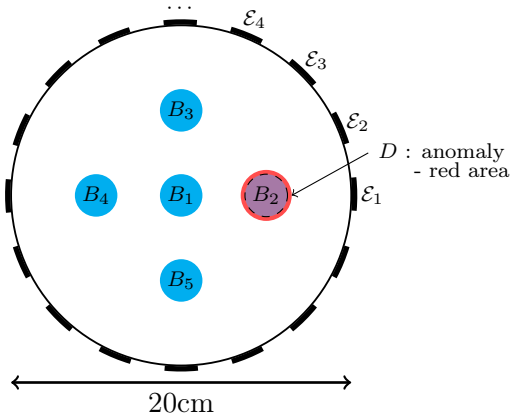


**Figure 1.** Measurement setting of example 4.1.

resp.,

$$g^* [R((1 - \beta\chi_B)\gamma_0) - \Re(\alpha R(\gamma_\omega))] g > 0,$$

so that

$$\Re(\alpha R(\gamma_\omega)) \not\leq R((1 + \beta\chi_B)\gamma_0), \quad \text{resp.,} \quad \Re(\alpha R(\gamma_\omega)) \not\geq R((1 - \beta\chi_B)\gamma_0).$$

□

#### 4. Numerical results

In this section, we numerically demonstrate our new method for the practically relevant electrode setting of Section 3.1. In all of the following settings,  $m$  electrodes  $\mathcal{E}_1, \mathcal{E}_2, \dots, \mathcal{E}_m$  are numbered as shown in the corresponding figures, and adjacent-adjacent dipole driving patterns are used according to this numbering, i.e., in the notation of section 3.1,

$$(j_r, k_r) := (r, r + 1) \quad \text{for } r = 1, \dots, m - 1, \quad \text{and} \quad (j_m, k_m) := (m, 1).$$

The EIT measurements at zero and non-zero frequency, and with and without ultrasound-modulation, are simulated by solving the equations (11)-(14) using MATLAB® and the commercial FEM-software COMSOL®.

At this point, let us stress again, that in a practical application of our new method, all required quantities are measured and no numerical simulations have to be carried out.

**Example 4.1.** Consider the setting illustrated in figure 1. The imaging domain  $\Omega$  is a two-dimensional circle with radius 10 centered at  $(0,0)$  and a circular anomaly  $D$  (sketched in red in figure 1) with radius 1.5 is located at  $(5,0)$ . On the boundary  $\partial\Omega$ , there are 16 electrodes  $\mathcal{E}_1, \mathcal{E}_2, \dots, \mathcal{E}_{16}$  attached.

$B_1$	$B_2$	$B_3$	$B_4$	$B_5$
-0.0024 ± 0.0005	0.0000 ± 0.0005	-0.0098 ± 0.0005	-0.0105 ± 0.0005	-0.0098 ± 0.0005
-0.0024 ± 0.0005	0.0000 ± 0.0005	-0.0097 ± 0.0005	-0.0104 ± 0.0005	-0.0097 ± 0.0005
-0.0000 ± 0.0005	0.0000 ± 0.0005	-0.0003 ± 0.0005	-0.0004 ± 0.0005	-0.0003 ± 0.0005
-0.0000 ± 0.0005	0.0000 ± 0.0005	-0.0002 ± 0.0005	-0.0003 ± 0.0005	-0.0002 ± 0.0005
-0.0000 ± 0.0005	0.0000 ± 0.0005	-0.0000 ± 0.0005	-0.0000 ± 0.0005	-0.0000 ± 0.0005
-0.0000 ± 0.0005	0.0000 ± 0.0005	-0.0000 ± 0.0005	-0.0000 ± 0.0005	-0.0000 ± 0.0005
-0.0000 ± 0.0005	0.0000 ± 0.0005	-0.0000 ± 0.0005	-0.0000 ± 0.0005	-0.0000 ± 0.0005
-0.0000 ± 0.0005	0.0000 ± 0.0005	-0.0000 ± 0.0005	-0.0000 ± 0.0005	-0.0000 ± 0.0005
-0.0000 ± 0.0005	0.0000 ± 0.0005	-0.0000 ± 0.0005	-0.0000 ± 0.0005	-0.0000 ± 0.0005
0.0000 ± 0.0005	0.0000 ± 0.0005	0.0000 ± 0.0005	0.0000 ± 0.0005	0.0000 ± 0.0005
0.0000 ± 0.0005	0.0000 ± 0.0005	0.0000 ± 0.0005	0.0000 ± 0.0005	0.0000 ± 0.0005
0.0003 ± 0.0005	0.0004 ± 0.0005	0.0005 ± 0.0005	0.0007 ± 0.0005	0.0005 ± 0.0005
0.0006 ± 0.0005	0.0005 ± 0.0005	0.0007 ± 0.0005	0.0009 ± 0.0005	0.0007 ± 0.0005
0.0142 ± 0.0005	0.0048 ± 0.0005	0.0146 ± 0.0005	0.0153 ± 0.0005	0.0146 ± 0.0005
0.0145 ± 0.0005	0.0049 ± 0.0005	0.0148 ± 0.0005	0.0155 ± 0.0005	0.0148 ± 0.0005

**Table 1.** Eigenvalues of  $R((1 + \beta\chi_{B_j})\gamma_0) - \Re(\alpha R(\gamma_\omega))$ ,  $j = 1, \dots, 5$ , for example 4.1.

The DC and AC admittivities  $\gamma_0$  and  $\gamma_\omega$  are chosen as

$$\gamma_0 := 1, \quad \text{and} \quad \gamma_\omega := \begin{cases} 1 + i\omega & \text{in } \Omega \setminus D, \\ 1 + 2i\omega & \text{in } D, \end{cases}$$

with  $\omega = 200\pi$ , i.e.  $\sigma_\Omega = \sigma_D = 1$ ,  $\epsilon_\Omega = 1$ , and  $\epsilon_D = 2$ . Hence, the ratio of the background conductivities is  $\alpha = 1 + i\omega$ , and the contrast assumption in theorem 3.2 is fulfilled with  $c = \epsilon_D\sigma_\Omega - \epsilon_\Omega\sigma_D = 1$ .

Theorem 3.2 guarantees that

$$B \subseteq D \quad \text{implies that} \quad \Re(\alpha R(\gamma_\omega)) \leq R((1 + \beta\chi_B)\gamma_0), \quad (17)$$

i.e., that the ultrasound modulated DC measurements  $R((1 + \beta\chi_B)\gamma_0)$  are larger (in the sense of matrix definiteness) than (the real part of ratio-weighted) AC measurements  $\Re(\alpha R(\gamma_\omega))$  if the ultrasound-modulated focusing region  $B$  lies inside the inclusion  $D$ , and the modulation strength  $\beta > 0$  is small enough. Remark 3.3 suggests that the converse of (17) is true if enough electrodes are used. To test this numerically, we choose 5 circular focusing regions  $B_1, \dots, B_5$  (sketched in blue in figure 1) with radius 1.25. The modulation strength is chosen to be (cf. theorem 3.2)

$$\beta = \omega^2 |c| \frac{\epsilon_\Omega}{\sigma_D(\sigma_\Omega^2 + \omega^2 \epsilon_\Omega^2)} \approx 0.9999.$$

Table 1 shows the eigenvalues of  $R((1 + \beta\chi_{B_j})\gamma_0) - \Re(\alpha R(\gamma_\omega))$  for  $j \in \{1, \dots, 5\}$ . The numerical error ( $\delta \approx 0.0005$ ) in table 1 was estimated by repeating the calculations on a finer FEM grid. Taking into account this estimated numerical error, the monotonicity test  $R((1 + \beta\chi_{B_j})\gamma_0) \geq \Re(\alpha R(\gamma_\omega))$  is only fulfilled for the focusing region  $B_2$ , which lies inside the inclusion.

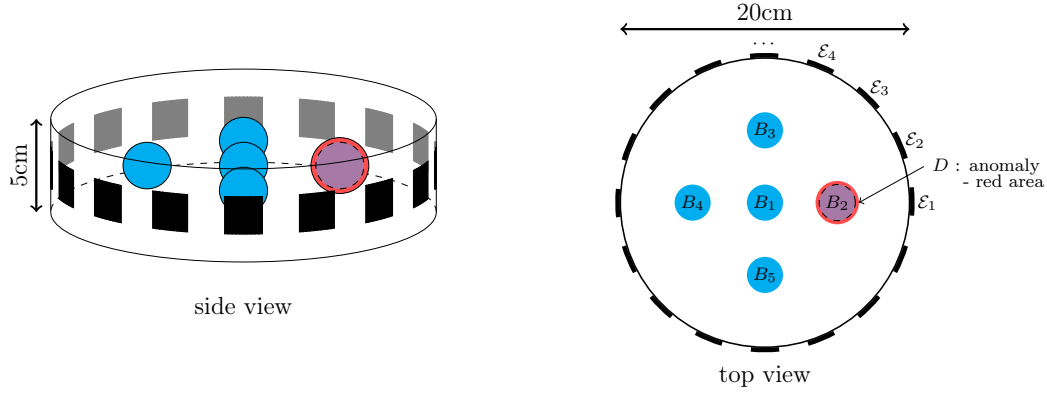


**Figure 2.** Measurement setting of example 4.2.

**Example 4.2.** Now we consider the three-dimensional setting illustrated in Figure 2. The imaging domain  $\Omega$  is a cylindrical domain with

$$\Omega = \{(x_1, x_2, x_3) \in \mathbb{R}^3 : \|(x_1, x_2, 0)\| < 10, 0 < x_3 < 5\}.$$

and a ball-shaped anomaly  $D$  with radius 1.5 is located at  $(5, 0, 2.5)$ . On the boundary  $\partial\Omega$ , there are 16 electrodes  $\mathcal{E}_1, \mathcal{E}_2, \dots, \mathcal{E}_{16}$  attached.

The DC and AC admittivities  $\gamma_0$  and  $\gamma_\omega$  are chosen as

$$\gamma_0 := \begin{cases} 1, & \text{in } \Omega \setminus D, \\ 2, & \text{in } D, \end{cases} \quad \text{and} \quad \gamma_\omega := \begin{cases} 1 + i\omega, & \text{in } \Omega \setminus D, \\ 2 + i\omega, & \text{in } D, \end{cases}$$

with  $\omega = 200\pi$ , so that  $\alpha = 1 + i\omega$  and  $c = -1$ . As in example 4.1 we check the monotonicity relation for five focusing regions  $B_1, B_2, B_3, B_4$  and  $B_5$ . The regions are ball-shaped with radius 1.25 and centered at  $(0, 0, 2.5), (5, 0, 2.5), (0, 5, 2.5), (-5, 0, 2.5)$  and  $(0, -5, 2.5)$ , respectively. We choose  $\beta$  according to theorem 3.2 as

$$\beta = \omega^2 |c| \frac{\epsilon_D}{\sigma_D(\sigma_D \sigma_\Omega + \omega^2 \epsilon_D \epsilon_\Omega)} \approx 0.4999.$$

Table 2 shows the eigenvalues of  $R((1 - \beta \chi_{B_j})\gamma_0) - \Re(\alpha R(\gamma_\omega))$  for  $j = \{1, \dots, 5\}$ . The numerical error ( $\delta \approx 0.14$ ) in table 2 was estimated by repeating the calculations on a finer FEM grid. Taking into account this estimated numerical error, the monotonicity test  $R((1 - \beta \chi_{B_j})\gamma_0) \leq \Re(\alpha R(\gamma_\omega))$  is only fulfilled for the second focussing region, which lies inside the inclusion.

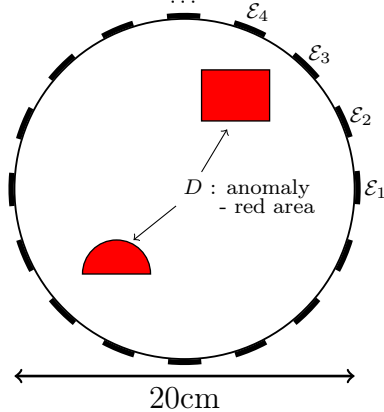
**Example 4.3.** In our last example we test a large number of small balls in order to demonstrate up to which extend the method is capable of determining the shape of an inclusion. We consider the two- and three-dimensional example shown in figure 3, and 4, respectively. In both settings,

$$\gamma_0 := 1, \quad \text{and} \quad \gamma_\omega := \begin{cases} 1 + 2i\omega & \text{in } \Omega \setminus D, \\ 1 + i\omega & \text{in } D, \end{cases}$$

with  $\omega = 200\pi$ , so that  $\alpha = 1 + 2i\omega$  and  $c = -1$ . In accordance with theorem 3.2, we choose

$$\beta = \omega^2 |c| \frac{\epsilon_D}{\sigma_D(\sigma_D \sigma_\Omega + \omega^2 \epsilon_D \epsilon_\Omega)} \approx 0.4999.$$

$B_1$	$B_2$	$B_3$	$B_4$	$B_5$
-0.1639 ± 0.0136	-0.0800 ± 0.0136	-0.1667 ± 0.0136	-0.1723 ± 0.0136	-0.1668 ± 0.0136
-0.1621 ± 0.0136	-0.0785 ± 0.0136	-0.1642 ± 0.0136	-0.1696 ± 0.0136	-0.1642 ± 0.0136
-0.0052 ± 0.0136	-0.0054 ± 0.0136	-0.0065 ± 0.0136	-0.0079 ± 0.0136	-0.0065 ± 0.0136
-0.0034 ± 0.0136	-0.0041 ± 0.0136	-0.0045 ± 0.0136	-0.0060 ± 0.0136	-0.0045 ± 0.0136
-0.0001 ± 0.0136	-0.0003 ± 0.0136	-0.0002 ± 0.0136	-0.0003 ± 0.0136	-0.0002 ± 0.0136
-0.0000 ± 0.0136	-0.0001 ± 0.0136	-0.0000 ± 0.0136	-0.0001 ± 0.0136	-0.0000 ± 0.0136
-0.0000 ± 0.0136	-0.0000 ± 0.0136	-0.0000 ± 0.0136	-0.0000 ± 0.0136	-0.0000 ± 0.0136
-0.0000 ± 0.0136	-0.0000 ± 0.0136	-0.0000 ± 0.0136	-0.0000 ± 0.0136	-0.0000 ± 0.0136
-0.0000 ± 0.0136	-0.0000 ± 0.0136	-0.0000 ± 0.0136	0.0000 ± 0.0136	-0.0000 ± 0.0136
0.0000 ± 0.0136	-0.0000 ± 0.0136	0.0000 ± 0.0136	0.0000 ± 0.0136	0.0000 ± 0.0136
0.0000 ± 0.0136	-0.0000 ± 0.0136	0.0000 ± 0.0136	0.0000 ± 0.0136	0.0000 ± 0.0136
0.0000 ± 0.0136	-0.0000 ± 0.0136	0.0000 ± 0.0136	0.0001 ± 0.0136	0.0000 ± 0.0136
0.0001 ± 0.0136	-0.0000 ± 0.0136	0.0011 ± 0.0136	0.0019 ± 0.0136	0.0011 ± 0.0136
0.0001 ± 0.0136	0.0000 ± 0.0136	0.0017 ± 0.0136	0.0025 ± 0.0136	0.0017 ± 0.0136
0.0169 ± 0.0136	0.0000 ± 0.0136	0.0728 ± 0.0136	0.0788 ± 0.0136	0.0717 ± 0.0136
0.0173 ± 0.0136	0.0000 ± 0.0136	0.0749 ± 0.0136	0.0822 ± 0.0136	0.0753 ± 0.0136

**Table 2.** Eigenvalues of  $R((1 - \beta\chi_{B_j})\gamma_0) - \Re(\alpha R(\gamma_\omega))$ ,  $j = 1, \dots, 5$ , for example 4.2.**Figure 3.** Two-dimensional measurement setting of example 4.3.

We now consider a large number of test balls  $B_j$ ,  $j \in \{1, 2, \dots, N\}$ , and mark all balls for which

$$R((1 - \beta\chi_{B_j})\gamma_0) - \Re(\alpha R(\gamma_\omega)) \leq \delta I, \quad (18)$$

where  $I$  is the identity matrix and  $\delta > 0$  is a regularization parameter. In both examples, we used the heuristically chosen value  $\delta = 0.5 \cdot 10^{-7}$ . Figure 5 and figure 6 show the test balls (in blue), the true inclusion (in red) and the balls for which (18) is fulfilled (in grey).

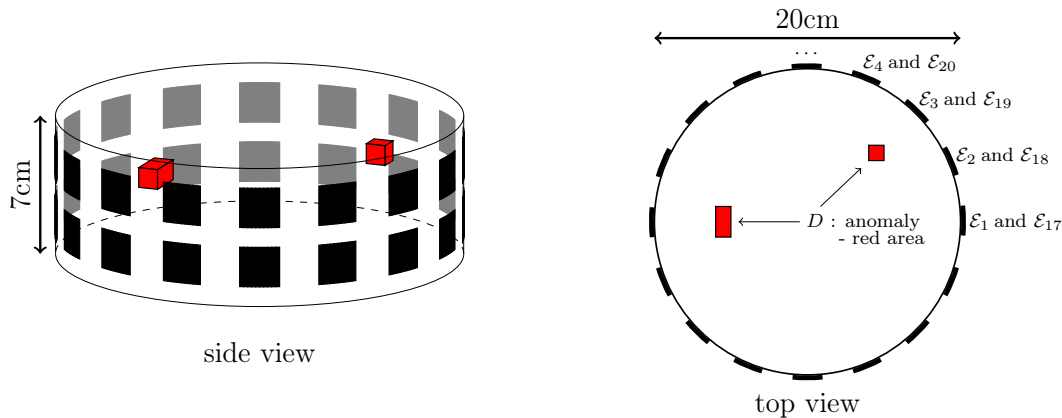


**Figure 4.** Three-dimensional measurement setting of example 4.3.

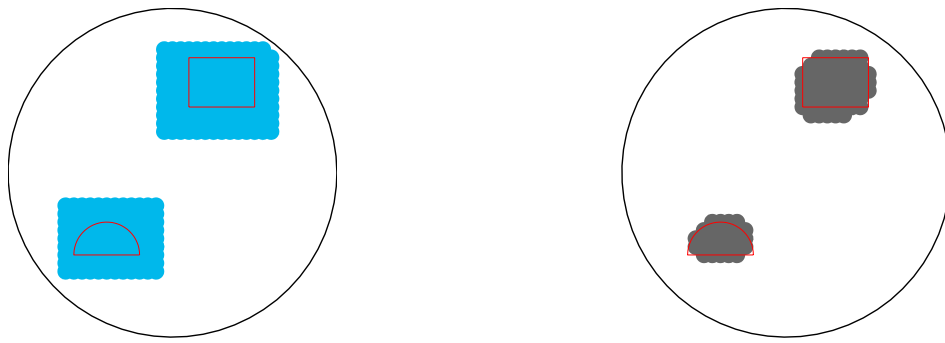


**Figure 5.** Results for the two-dimensional setting in example 4.3.

## 5. Conclusion and discussion

We have developed a new method to detect and localize conductivity anomalies by combining frequency-difference electrical impedance tomography (EIT) with ultrasound-modulated EIT. Our method is based on comparing (in terms of matrix definiteness) ultrasound-modulated EIT measurements with (the real part of ratio-weighted) EIT measurements at a non-zero frequency. We showed that this comparison determines whether the focusing region of the ultrasound wave lies inside a conductivity anomaly or not.

Remarkably, our new method merely utilizes the two sets of EIT measurements, and the background conductivity ratio which in turn can be estimated from EIT measurements. The method does not require any numerical simulations, forward calculations or geometry-dependent special solutions. It can be implemented without knowing the imaging domain shape or the electrode position, and is thus completely unaffected by modeling errors.

We gave a rigorous mathematical proof for our new method for the case of continuous boundary data, and we justified why the method can be expected to work also for realistic electrode measurements, provided that the number of electrodes is large enough.

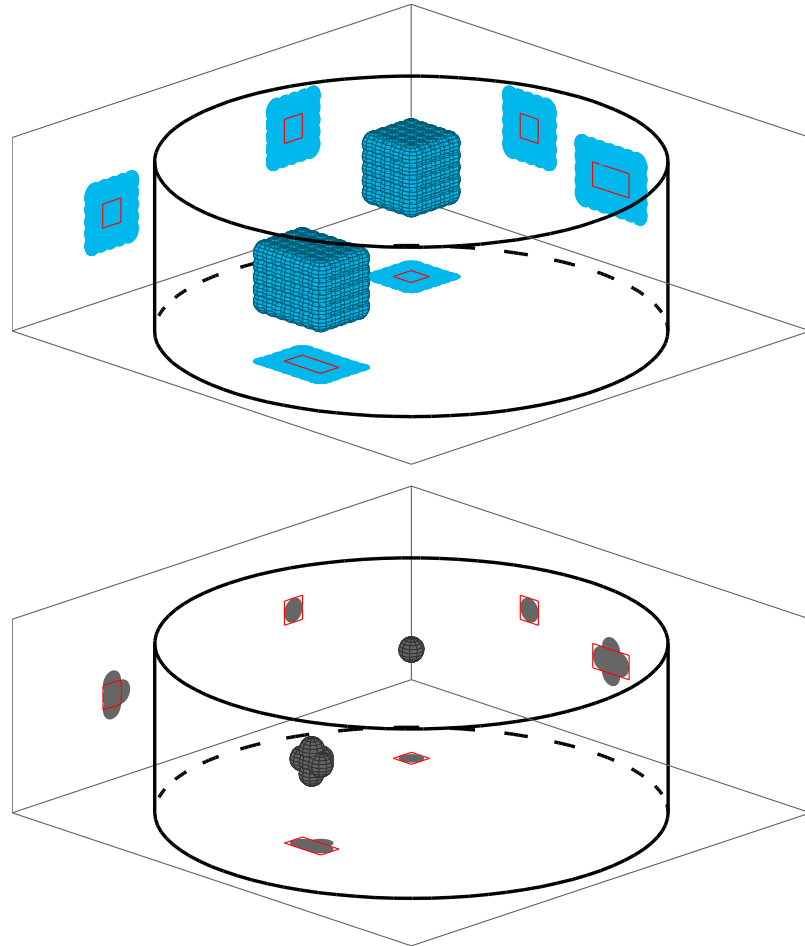


**Figure 6.** Results for the three-dimensional setting in example 4.3.

The method is based on the assumption that the background conductivity is spatially constant, and that the anomalies fulfill the contrast condition that is required in frequency-difference EIT. Also, our method relies on the idealistic assumption of ultrasound modulated EIT, that it is possible to perfectly focus an ultrasound wave so that the conductivity changes only in a small test region. In real applications, background conductivities can be expected to be at least slightly inhomogeneous, and the ultrasound wave will also have some effect on the conductivity outside the focusing region. The performance of our new method in such a setting has yet to be evaluated. Let us however note that the matrix definiteness comparisons, that are used by our method, are principally stable (cf. remark 2.3) so that our arguably idealistic modeling assumptions only have to be approximately valid. Moreover, monotonicity arguments also allow for worst-case testing and resolution guarantees (cf. [37]) which might be helpful in relaxing the idealistic assumptions in future studies.

## Acknowledgments

BH and MU would like to thank the German Research Foundation (DFG) for financial support of the project within the Cluster of Excellence in Simulation Technology (EXC 310/1) at the University of Stuttgart.

## References

- [1] A. Adler, R. Gaburro, and W. Lionheart. Electrical impedance tomography. In *Handbook of Mathematical Methods in Imaging*, pages 599–654. Springer, 2011.
- [2] H. Ammari, E. Bonnetier, Y. Capdeboscq, M. Tanter, M. Fink, et al. Electrical impedance tomography by elastic deformation. *SIAM Journal on Applied Mathematics*, 68(6):1557–1573, 2008.
- [3] H. Ammari, J. Garnier, and W. Jing. Resolution and stability analysis in acousto-electric imaging. *Inverse Problems*, 28(8):084005, 2012.
- [4] G. Bal. Cauchy problem for ultrasound-modulated eit. *Analysis & PDE*, 6(4):751–775, 2013.
- [5] G. Bal, W. Naetar, O. Scherzer, and J. Schotland. The levenberg-marquardt iteration for numerical inversion of the power density operator. *Journal of Inverse and Ill-Posed Problems*, 21(2):265–280, 2013.
- [6] D. Barber and B. Brown. Applied potential tomography. *J. Phys. E: Sci. Instrum.*, 17(9):723–733, 1984.
- [7] A. Barth, B. Harrach, N. Hyvönen, and L. Mustonen. Detecting stochastic inclusions in electrical impedance tomography. *Preprint, available online at www.mathematik.uni-stuttgart.de/oip*.
- [8] R. Bayford. Bioimpedance tomography (electrical impedance tomography). *Annu. Rev. Biomed. Eng.*, 8:63–91, 2006.
- [9] E. Bonnetier and F. Triki. A note on reconstructing the conductivity in impedance tomography by elastic perturbation. In *The Impact of Applications on Mathematics*, pages 275–282. Springer, 2014.
- [10] L. Borcea. Electrical impedance tomography. *Inverse Problems*, 18(6):99–136, 2002.
- [11] L. Borcea. Addendum to ‘Electrical impedance tomography’. *Inverse Problems*, 19(4):997–998, 2003.
- [12] B. Brown. Electrical impedance tomography (EIT): a review. *J Med Eng Technol.*, 27(3):97–108, 2003.
- [13] B. Brown and A. Seagar. The sheffield data collection system. *Clinical Physics and Physiological Measurement*, 8(4A):91, 1987.
- [14] M. Brühl and M. Hanke. Numerical implementation of two noniterative methods for locating inclusions by impedance tomography. *Inverse Problems*, 16(4):1029–1042, 2000.
- [15] N. Chaulet, S. Arridge, T. Betcke, and D. Holder. The factorization method for three dimensional electrical impedance tomography. *Inverse Problems*, 30(4):045005, 2014.
- [16] M. Cheney, D. Isaacson, and J. C. Newell. Electrical impedance tomography. *SIAM Rev.*, 41(1):85–101, 1999.
- [17] M. K. Choi, B. Harrach, and J. K. Seo. Regularizing a linearized eit reconstruction method using a sensitivity-based factorization method. *Inverse Problems in Science and Engineering*, 22(7):1029–1044, 2014.
- [18] E. T. Chung, T. F. Chan, and X.-C. Tai. Electrical impedance tomography using level set representation and total variational regularization. *Journal of Computational Physics*, 205(1):357–372, 2005.
- [19] O. Dorn and D. Lesselier. Level set methods for inverse scattering. *Inverse Problems*, 22(4):R67, 2006.

- [20] A. Friedman. Detection of mines by electric measurements. *SIAM J. Appl. Math.*, 47(1):201–212, 1987.
- [21] A. Friedman and V. Isakov. On the uniqueness in the inverse conductivity problem with one measurement. *Indiana Univ. Math. J.*, 38(3):563–579, 1989.
- [22] B. Gebauer. The factorization method for real elliptic problems. *Z. Anal. Anwendungen*, 25:81–102, 2006.
- [23] B. Gebauer. Localized potentials in electrical impedance tomography. *Inverse Probl. Imaging*, 2(2):251–269, 2008.
- [24] B. Gebauer and N. Hyvönen. Factorization method and irregular inclusions in electrical impedance tomography. *Inverse Problems*, 23:2159–2170, 2007.
- [25] B. Gebauer and O. Scherzer. Impedance-acoustic tomography. *SIAM J. Appl. Math.*, 69:565–576, 2008.
- [26] H. Haddar and G. Migliorati. Numerical analysis of the factorization method for eit with a piecewise constant uncertain background. *Inverse Problems*, 29(6):065009, 2013.
- [27] H. Hakula and N. Hyvönen. On computation of test dipoles for factorization method. *BIT*, 49(1):75–91, 2009.
- [28] M. Hanke and M. Brühl. Recent progress in electrical impedance tomography. *Inverse Problems*, 19:S65–S90, 2003.
- [29] M. Hanke, B. Harrach, and N. Hyvönen. Justification of point electrode models in electrical impedance tomography. *Mathematical Models and Methods in Applied Sciences*, 21(06):1395–1413, 2011.
- [30] M. Hanke and A. Kirsch. Sampling methods. In O. Scherzer, editor, *Handbook of Mathematical Models in Imaging*, pages 501–550. Springer, 2011.
- [31] M. Hanke and B. Schappel. The factorization method for electrical impedance tomography in the half-space. *SIAM J. Appl. Math.*, 68(4):907–924, 2008.
- [32] B. Harrach. Interpolation of missing electrode data in electrical impedance tomography. *Preprint, available online at www.mathematik.uni-stuttgart.de/oip*.
- [33] B. Harrach. Recent progress on the factorization method for electrical impedance tomography. *Computational and mathematical methods in medicine*, 2013, 2013.
- [34] B. Harrach and J. K. Seo. Detecting inclusions in electrical impedance tomography without reference measurements. *SIAM Journal on Applied Mathematics*, 69(6):1662–1681, 2009.
- [35] B. Harrach and J. K. Seo. Exact shape-reconstruction by one-step linearization in electrical impedance tomography. *SIAM Journal on Mathematical Analysis*, 42(4):1505–1518, 2010.
- [36] B. Harrach, J. K. Seo, and E. J. Woo. Factorization method and its physical justification in frequency-difference electrical impedance tomography. *IEEE Trans. Med. Imaging*, 29(11):1918–1926, 2010.
- [37] B. Harrach and M. Ullrich. Resolution guarantees in electrical impedance tomography. *To appear in IEEE Trans. Med. Imaging*.
- [38] B. Harrach and M. Ullrich. Monotonicity-based shape reconstruction in electrical impedance tomography. *SIAM Journal on Mathematical Analysis*, 45(6):3382–3403, 2013.
- [39] R. Henderson and J. Webster. An impedance camera for spatially specific measurements of the thorax. *IEEE Trans. Biomed. Eng.*, BME-25(3):250–254, 1978.
- [40] D. Holder. *Electrical Impedance Tomography: Methods, History and Applications*. IOP Publishing, Bristol, UK, 2005.
- [41] N. Hyvönen. Complete electrode model of electrical impedance tomography: Approximation properties and characterization of inclusions. *SIAM Journal on Applied Mathematics*, 64(3):902–931, 2004.
- [42] N. Hyvönen. Approximating idealized boundary data of electric impedance tomography by electrode measurements. *Mathematical Models and Methods in Applied Sciences*, 19(07):1185–1202, 2009.
- [43] N. Hyvönen, H. Hakula, and S. Pursiainen. Numerical implementation of the factorization

- method within the complete electrode model of electrical impedance tomography. *Inverse Probl. Imaging*, 1(2):299–317, 2007.
- [44] T. Ide, H. Isozaki, S. Nakata, and S. Siltanen. Local detection of three-dimensional inclusions in electrical impedance tomography. *Inverse problems*, 26:035001, 2010.
  - [45] T. Ide, H. Isozaki, S. Nakata, S. Siltanen, and G. Uhlmann. Probing for electrical inclusions with complex spherical waves. *Comm. Pure Appl. Math.*, 60:1415–1442, 2007.
  - [46] M. Ikehata. Size estimation of inclusion. *J. Inverse Ill-Posed Probl.*, 6(2):127–140, 1998.
  - [47] M. Ikehata. How to draw a picture of an unknown inclusion from boundary measurements. Two mathematical inversion algorithms. *J. Inverse Ill-Posed Probl.*, 7(3):255–271, 1999.
  - [48] M. Ikehata. Reconstruction of the support function for inclusion from boundary measurements. *J. Inverse Ill-Posed Probl.*, 8(4):367–378, 2000.
  - [49] M. Ikehata. A regularized extraction formula in the enclosure method. *Inverse Problems*, 18(2):435, 2002.
  - [50] M. Ikehata and S. Siltanen. Numerical method for finding the convex hull of an inclusion in conductivity from boundary measurements. *Inverse Problems*, 16(4):1043–1052, 2000.
  - [51] M. Ikehata and S. Siltanen. Electrical impedance tomography and Mittag-Leffler’s function. *Inverse Problems*, 20:1325, 2004.
  - [52] K. Ito, K. Kunisch, and Z. Li. Level-set function approach to an inverse interface problem. *Inverse problems*, 17(5):1225, 2001.
  - [53] H. Kang, J. K. Seo, and D. Sheen. The inverse conductivity problem with one measurement: stability and estimation of size. *SIAM J. Math. Anal.*, 28(6):1389–1405, 1997.
  - [54] A. Kirsch. The factorization method for a class of inverse elliptic problems. *Math. Nachr.*, 278(3):258–277, 2005.
  - [55] A. Kirsch and N. Grinberg. *The Factorization Method for Inverse Problems*, volume 36 of *Oxford Lecture Ser. Math. Appl.* Oxford University Press, Oxford, 2007.
  - [56] I. Kocyigit. Acousto-electric tomography and CGO solutions with internal data. *Inverse Problems*, 28(12):125004, 2012.
  - [57] P. Kuchment. Mathematics of hybrid imaging: A brief review. In *The Mathematical Legacy of Leon Ehrenpreis*, pages 183–208. Springer, 2012.
  - [58] P. Kuchment and L. Kunyansky. 2D and 3D reconstructions in acousto-electric tomography. *Inverse Problems*, 27(5):055013, 2011.
  - [59] A. Lechleiter, N. Hyvönen, and H. Hakula. The factorization method applied to the complete electrode model of impedance tomography. *SIAM Journal on Applied Mathematics*, 68(4):1097–1121, 2008.
  - [60] W. R. B. Lionheart. EIT reconstruction algorithms: pitfalls, challenges and recent developments. *Physiol. Meas.*, 25:125–142, 2004.
  - [61] P. Metherall, D. C. Barber, R. H. Smallwood, and B. H. Brown. Three-dimensional electrical impedance tomography. *Nature*, 380:509–512, 1996.
  - [62] F. Monard and G. Bal. Inverse anisotropic conductivity from power densities in dimension  $n \geq 3$ . *Communications in Partial Differential Equations*, 38(7):1183–1207, 2013.
  - [63] A. I. Nachman, L. Päivärinta, and A. Teirilä. On imaging obstacles inside inhomogeneous media. *J. Funct. Anal.*, 252(2):490–516, 2007.
  - [64] D. Nguyen, C. Jin, A. Thiagalingam, and A. McEwan. A review on electrical impedance tomography for pulmonary perfusion imaging. *Physiol. Meas.*, 33(5):695–706, 2012.
  - [65] R. Potthast. A survey on sampling and probe methods for inverse problems. *Inverse Problems*, 22(2):R1–R47, 2006.
  - [66] P. Rahmati, M. Soleimani, S. Pulletz, I. Frerichs, and A. Adler. Level-set-based reconstruction algorithm for EIT lung images: first clinical results. *Physiol. Meas.*, 33(5):739, 2012.
  - [67] S. Schmitt. The factorization method for EIT in the case of mixed inclusions. *Inverse Problems*, 25:065012, 2009.
  - [68] S. Schmitt and A. Kirsch. A factorization scheme for determining conductivity contrasts in

- impedance tomography. *Inverse Problems*, 27:095005, 2011.
- [69] J. K. Seo, J. Lee, H. Zribi, S. W. Kim, and E. J. Woo. Frequency-difference electrical impedance tomography (fdEIT): Algorithm development and feasibility study. *Physiol. Meas.*, 29:929–944, 2008.
  - [70] M. Soleimani. Electrical impedance tomography imaging using a priori ultrasound data. *Biomedical engineering online*, 5(1):8, 2006.
  - [71] G. Steiner, M. Soleimani, and D. Watzenig. A bio-electromechanical imaging technique with combined electrical impedance and ultrasound tomography. *Physiological measurement*, 29(6):S63, 2008.
  - [72] X.-C. Tai and T. F. Chan. A survey on multiple level set methods with applications for identifying piecewise constant functions. *Int. J. Num. Anal. Model.*, 1(1):25–47, 2004.
  - [73] A. Tamburrino. Monotonicity based imaging methods for elliptic and parabolic inverse problems. *J. Inverse Ill-Posed Probl.*, 14(6):633–642, 2006.
  - [74] A. Tamburrino and G. Rubinacci. A new non-iterative inversion method for electrical resistance tomography. *Inverse Problems*, 18(6):1809–1829, 2002.
  - [75] G. Uhlmann. Electrical impedance tomography and Calderón’s problem. *Inverse Problems*, 25(12):123011, 2009.
  - [76] G. Uhlmann and J. Wang. Reconstructing discontinuities using complex geometrical optics solutions. *SIAM J. Appl. Math.*, 68:1026, 2008.
  - [77] K. van den Doel and U. M. Ascher. On level set regularization for highly ill-posed distributed parameter estimation problems. *Journal of Computational Physics*, 216(2):707–723, 2006.
  - [78] T. Widlak and O. Scherzer. Hybrid tomography for conductivity imaging. *Inverse Problems*, 28(8):084008, 2012.
  - [79] H. Zhang and L. V. Wang. Acousto-electric tomography. In *Biomedical Optics 2004*, pages 145–149. International Society for Optics and Photonics, 2004.
  - [80] L. Zhou, B. Harrach, and J. K. Seo. Monotonicity-based electrical impedance tomography lung imaging. *Preprint, available online at [www.mathematik.uni-stuttgart.de/oip](http://www.mathematik.uni-stuttgart.de/oip).*